

A total-strain based orthotropic continuum model for the cyclic nonlinear behavior of unreinforced brick masonry structures

Sousamli, Marianthi; Messali, Francesco; Rots, Jan G.

DOI

[10.1002/nme.6917](https://doi.org/10.1002/nme.6917)

Publication date

2022

Document Version

Final published version

Published in

International Journal for Numerical Methods in Engineering

Citation (APA)

Sousamli, M., Messali, F., & Rots, J. G. (2022). A total-strain based orthotropic continuum model for the cyclic nonlinear behavior of unreinforced brick masonry structures. *International Journal for Numerical Methods in Engineering*, 123(8), 1813-1840. <https://doi.org/10.1002/nme.6917>

Important note

To cite this publication, please use the final published version (if applicable). Please check the document version above.

Copyright

Other than for strictly personal use, it is not permitted to download, forward or distribute the text or part of it, without the consent of the author(s) and/or copyright holder(s), unless the work is under an open content license such as Creative Commons.

Takedown policy

Please contact us and provide details if you believe this document breaches copyrights. We will remove access to the work immediately and investigate your claim.

A total-strain based orthotropic continuum model for the cyclic nonlinear behavior of unreinforced brick masonry structures

Marianthi Sousamli¹ | Francesco Messali | Jan G. Rots

Faculty of Civil Engineering & Geosciences, TU Delft, Delft, The Netherlands

Correspondence

Marianthi Sousamli, Faculty of Civil Engineering & Geosciences, TU Delft, Delft, The Netherlands.
Email: m.sousamli@tudelft.nl

Funding information

Nederlandse Aardolie Maatschappij (NAM)

Abstract

Plane-stress and shell macromodels are often preferred to analyze masonry structures because of their numerical efficiency. However, they often misestimate the hysteretic behavior of the structures. Additionally, due to the nature of smeared cracks, the cracks may be diffused. This article proposes a new orthotropic model, which focuses on the cyclic, nonlinear behavior of brick masonry structures. The model adopts a total-strain based rotating crack approach. It describes tensile and compressive failure in the rotating principal directions, while including indirectly shear failure through an internal iterative algorithm. Two distinctions are made regarding the tensile postpeak and unloading/reloading behavior based on the crack orientation at crack initiation: a steep softening branch and secant unloading are adopted when the crack angle corresponds to in-plane flexural failure, and a softening branch and bilinear unloading are adopted when the crack angle corresponds to diagonal shear failure. Bilinear unloading/reloading is adopted in compression, resulting in a cyclic behavior resembling shear. The constitutive model was implemented in a finite element software and validated against experimental results. The numerical simulations reproduced well the experimental outcomes in terms of envelope load-displacement curve and hysteretic behavior, while simultaneously they resulted in localized damage, representative of the experimental crack patterns.

KEYWORDS

constitutive model, continuum fracture mechanics, damage localization, macromodeling, shear failure, unreinforced masonry

1 | INTRODUCTION

Masonry is one of the oldest building materials in the world. Due to its aesthetics, availability and ease of construction, it is found in many structures around the world, from historic monuments to residential buildings. It consists of units, such as bricks, stones or blocks, and joints, dry or mortar, arranged in a geometrical pattern. The different material properties of these constituents as well as their geometric arrangement make masonry an inhomogeneous and orthotropic material.

This is an open access article under the terms of the Creative Commons Attribution License, which permits use, distribution and reproduction in any medium, provided the original work is properly cited.

© 2022 The Authors. *International Journal for Numerical Methods in Engineering* published by John Wiley & Sons Ltd.

Thanks to the advances in the field of numerical methods, four different approaches have been developed for the numerical modeling of masonry structures: macroelement based methods, like the lumped mass approach and the equivalent frame method,¹⁻³ discrete element methods (DEM),⁴⁻⁷ finite element methods (FEM), and most recently hybrid methods, like the finite-discrete element methods (F-DEM)^{8,9} or the macro-distinct element (M-DEM).¹⁰ In FEM, which currently is the most commonly used approach, masonry is modeled according to two methods: the micromodeling, detailed or simplified, and the macromodeling approach. According to micromodeling every unit/brick (and every mortar joint in the case of detailed micromodeling) is modeled individually with its real geometrical and material properties, and it is connected to its surroundings through discontinuous interface elements.¹¹⁻¹⁴ On the other hand, in the macromodeling (or continuum models) approach, masonry is considered to be a homogeneous material and the damage is distributed over the continuum. Macromodels can be based either on direct approaches, where the constitutive equations and material properties adopted should represent the behavior of masonry and should be obtained by tests performed on sufficiently large specimens, or on homogenization approaches (e.g., References 15-17), where the constitutive laws are derived through a homogenization process that relates the microscale material to the structural-scale. The micromodeling approach is more accurate and is better able to predict the hysteretic behavior and local failure mechanisms of a structure. However, it is computationally very demanding and its use, up to now, is mostly limited to simulating single structural elements, like walls. On the other hand, macromodels constitute a good compromise between accuracy and computational effort, and are often preferred for modeling large structures, in order to reduce the required computational time.

In order to increase the accuracy of direct macromodels, the orthotropy of the material needs to be included. Currently, a number of constitutive models are available for masonry, based on the frameworks of smeared cracking,^{18,19} damage mechanics,²⁰⁻²³ and plasticity.^{24,25} However, even though these models include orthotropy in the description of the mechanical behavior, more challenges need to be overcome. Firstly, predicted crack patterns are sometimes too diffuse: wide zones of smeared cracked Gauss points have been reported (e.g., References 18,20) rather than the localized discrete cracks identified in the last stages of tests. This is in part expected, since macromodels do not depict the exact geometry of a structure; however, a realistic damage localization is an important factor to consider when the structure needs to be strengthened. Secondly, most of the existing models have been validated only against experimental results of monotonic tests, whereas the few that have been validated against cyclic tests^{18,20,25} tend to underestimate the energy dissipation, especially in the case of shear walls. The cyclic hysteretic response may be partially missed because of the unloading/reloading characteristics of the existing models: either fully secant for damage/smeared cracking models or fully elastic for plasticity models. Damage-plasticity models tackle this issue, but even though such models have been developed for concrete (e.g., References 26,27), and a few attempts have been made for interface elements,^{11,14,28} only one is available for macromodeling of masonry.²⁵ Thirdly, existing models may not always estimate the postpeak part of the load-displacement response correctly, and in general models require the calibration of a large number of material input parameters to obtain accurate predictions. In summary, constitutive models for masonry have progressed significantly over the years, but their accuracy still needs to be improved.

This article presents a newly developed orthotropic, continuum constitutive model for macromodeling applications. The model belongs to the family of smeared crack/crush models and is based on a total-strain-rotating-crack (TSRC) approach. The novelty of the model lies on two things: first, the way in which shear failure is incorporated through an internal iterative algorithm; second, the unloading/reloading behavior that depends on the cracking angle at the onset of cracking and on the corresponding type of failure. In that way, secant unloading/reloading is adopted when cracking due to flexure occurs, and bilinear unloading/reloading when cracking/sliding due to shear or crushing occur. Moreover, it focuses on the nonlinear cyclic behavior of masonry and on improving the crack localization and hysteretic behavior of masonry structures. In order to validate its accuracy, the model is implemented in a FEM software and is used to simulate four unreinforced brick masonry walls, tested under cyclic, in-plane conditions. Subsequently, the numerical results are compared against the experimental results derived from the in-plane tests. The accuracy of the model is evaluated in terms of the envelope force-displacement curve, hysteretic response and energy dissipation, and in terms of crack patterns. It will be demonstrated that the developed model estimates well the base shear capacity of the walls and their postpeak behavior, whereas it predicts the correct failure mechanism and damage localization.

The newly developed model and its constitutive relations are presented in Section 2, whereas the validation of the model against experimental results is presented in Section 3. Mesh-sensitivity and other aspects of the model are discussed in Section 4. Finally, the concluding remarks are reported in Sections 5.

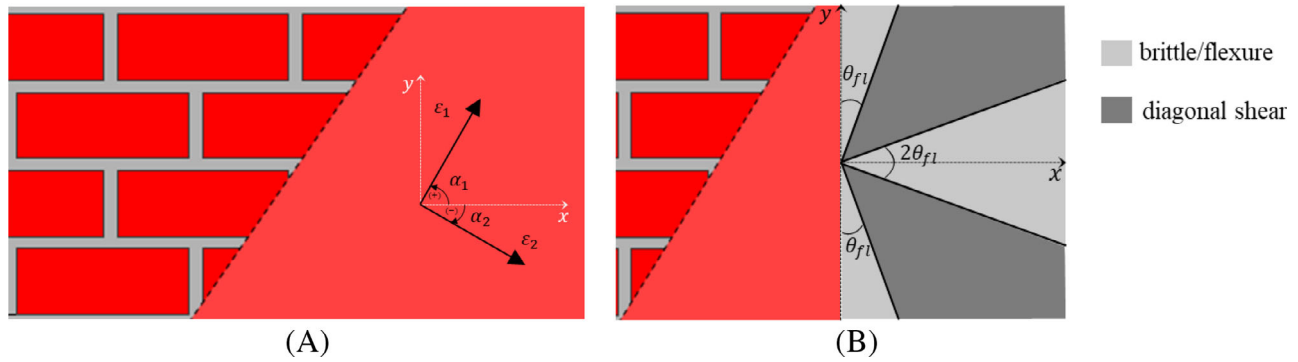


FIGURE 1 (A) Definition of principal directions and principal angles α_1 and α_2 ; (B) definition of threshold angle θ_{f1} and zones of assumed flexural and diagonal shear failure

2 | AN ORTHOTROPIC TOTAL-STRAIN BASED CRACK MODEL

The constitutive model presented in this paper is based on a TSRC concept²⁹ and it incorporates a number of newly implemented characteristics to make its application more suitable for masonry structures. The rotating crack concept describes the constitutive behavior in terms of stress–strain relations in the rotating principal axes. Coaxiality between principal stresses and strains is achieved through a shear stiffness term.¹⁹ A major advantage of rotating crack models over fixed crack models is that they eliminate the difficulty of choosing an appropriate shear retention factor, which can lead to unfavorable stress-locking in crack bands.³⁰ Moreover, they are usually relatively robust and easily comprehensible from an engineering point of view, since it is sufficient to describe the stress–strain relationships along the principal directions, and it is not required to deal with complicated concepts, such as return-mapping algorithms and corners in yield surfaces. The model is formulated in 2D plane stress, but extension to shell and 3D solid elements is possible.

As aforementioned, orthotropy is one of the main characteristics of masonry, being caused by the geometrical arrangement and the different material properties of its constituents. The developed model incorporates the orthotropic behavior through the different elastic and inelastic material properties, which are used to describe the constitutive relationships along the two principal directions i . In order to define the principal directions i , first a distinction should be made between isotropic and anisotropic materials; in isotropic materials, during the elastic phase, the principal direction of the strains coincides with the principal direction of the stresses. On the contrary, for anisotropic materials the principal directions of the stresses and strains are generally not aligned, but it rather depends on the particular elastic properties.

In the presented constitutive model, the principal directions i refer initially to the directions of the principal strains. Coaxiality is ensured through the adopted constitutive relationships. Therefore, the general term principal direction is used consistently both for stresses and strains. The angles α_i are defined as the angles inscribed by the line parallel to the bed joints and the line parallel to the principal strains ϵ_i , where $i = 1, 2$ is the index of the principal direction (Figure 1A). Due to the symmetric geometrical arrangement of brick masonry, it is sufficient to describe these angles within $-90^\circ \leq \alpha_i \leq 90^\circ$, as follows:

$$\alpha_1 = \begin{cases} \theta_1 & \text{if } |\theta_1 - \alpha_{1,0}| \leq 45^\circ \text{ or } |\theta_2 - \alpha_{2,0}| \leq 45^\circ \\ \theta_2 & \text{else} \end{cases}, \quad (1)$$

$$\alpha_2 = \begin{cases} \theta_1 & \text{if } \alpha_1 = \theta_2 \\ \theta_2 & \text{if } \alpha_1 = \theta_1 \end{cases} \quad (2)$$

with $\theta_1 = 0.5 \arctan\left(\frac{\gamma_{xy}}{\epsilon_{xx} - \epsilon_{yy}}\right)$ and $\theta_2 = \begin{cases} \theta_1 - 90^\circ & \text{if } \theta_1 \geq 0 \\ \theta_1 + 90^\circ & \text{if } \theta_1 < 0 \end{cases}$.

In the above equation, $\alpha_{i,0}$ refers to the angle in the principal direction i in the previous iteration step. Note that the angles θ_1, θ_2 relate to the directions of the principal strains too. However, since the model is orthotropic and focuses on the cyclic behavior of the material, the angles α_1 and α_2 as defined in Equations (1) and (2) are used to calculate the principal strains ϵ_1 and ϵ_2 . The term $|\theta_i - \alpha_{i,0}| \leq 45^\circ$ ensures that there is a gradual rotation of the principal

stresses/strains and that the correct material properties and cyclic behavior are assigned to each principal stress/strain component.

2.1 | Material properties and orthotropy

In order to define the orthotropic behavior of masonry, the material properties alongside its axes should be defined first. To do so, experiments are carried out for the characterization of masonry in tension, compression, and shear. Most authors (e.g., References 31-33) identify the compressive and tensile strengths and their corresponding fracture energies in the directions parallel and/or perpendicular to the bed joints. Additionally, the cohesion and the friction angle for loading parallel to the bed joints can be identified from shear tests.³⁴ Nevertheless, most experiments are limited to testing parallel to the mortar joints (especially to the head-joints) and there is a lack of mechanical data for loading in different directions. Given this lack of experimental data for different angles, the mechanical properties (with the exception of the tensile strength) are assumed to vary linearly with respect to the principal angles α_i .

Fifteen independent material parameters are required for the definition of the constitutive laws; these are properties defined by experiments carried out parallel to the bed joints (x direction) and head joints (y direction) and include: the Young's moduli ($E_{0,x}, E_{0,y}$), the shear modulus (G) the tensile strengths ($f_{t,x}, f_{t,y}$), the compressive strengths and their corresponding strains ($f_{c,x}, f_{c,y}, \epsilon_{pc,x}, \epsilon_{pc,y}$), as well as the fracture energies in tension ($G_{ft,x}, G_{ft,y}$), the fracture energies in compression ($G_{fc,x}, G_{fc,y}$), and finally the cohesion (c_0) and friction coefficient ($\tan \phi$) due to shear friction along the bed joint. The Young's moduli and the compressive strengths, strains, and fracture energies can be identified through compression tests, whereas the tensile strength and tensile fracture energy are typically identified through bond wrench tests and/or four-point bending tests. Nevertheless, due to masonry's brittle failure in tension, it is not always easy to measure fracture energy in tension,³⁵ in which case either representative values provided by guidelines³⁶ or derived by formulas,³⁷ or finally values retrieved indirectly from bending tests (indirect tension) can be used. The shear modulus can be calculated either through the Young's modulus and Poisson's ratios that are measured from compression tests, or it can be directly estimated as a fraction of the Young's modulus (40% according to Eurocode 6-part 1³⁸). Finally, the initial cohesion and friction coefficient are usually defined through shear tests on triplets.

As aforementioned, the experimental data provides little information regarding the material properties of brick masonry under different loading directions. Page^{33,39} has contributed on this by testing the biaxial tensile and compressive strength properties of brick masonry under different angles. However, further information about the elastic and other inelastic properties along different angles is still scarce. Therefore, it is assumed that the Young's moduli (E_i) (Figure 2A), the compressive strain ($\epsilon_{pc,i}$) corresponding to the compressive strength and the fracture energies in compression ($G_{fc,i}$) along the direction i vary linearly. For simplicity, linear variation is also assumed for the compressive strengths ($f_{c,i}$), although the information from the tests by Page suggests some nonlinear variation. Their definitions are given in Equations (3) to (6).

$$E_i = E_{0,x} + (E_{0,y} - E_{0,x}) \frac{|\alpha_i|}{90^\circ}, \quad (3)$$

$$f_{c,i} = f_{c,x} + (f_{c,y} - f_{c,x}) \frac{|\alpha_i|}{90^\circ}, \quad (4)$$

$$\epsilon_{pc,i} = \epsilon_{pc,x} + (\epsilon_{pc,y} - \epsilon_{pc,x}) \frac{|\alpha_i|}{90^\circ}, \quad (5)$$

$$G_{fc,i} = G_{fc,x} + (G_{fc,y} - G_{fc,x}) \frac{|\alpha_i|}{90^\circ}. \quad (6)$$

The tensile strength ($f_{t,i}$) along the principal direction i is defined such that it fits the experimental results obtained from Reference 33 for uniaxial tensile loading (Figure 2B). The corresponding formulation is described by

$$f_{t,i} = f_{t,x} - (f_{t,x} - f_{t,y}) \frac{|\alpha_i|}{90^\circ} + (f_{\max} - 0.5 (f_{t,x} + f_{t,y})) \sin(4 |\alpha_i|), \quad (7)$$

where $f_{\max} = \sqrt{f_{t,x}^2 + f_{t,y}^2}$.

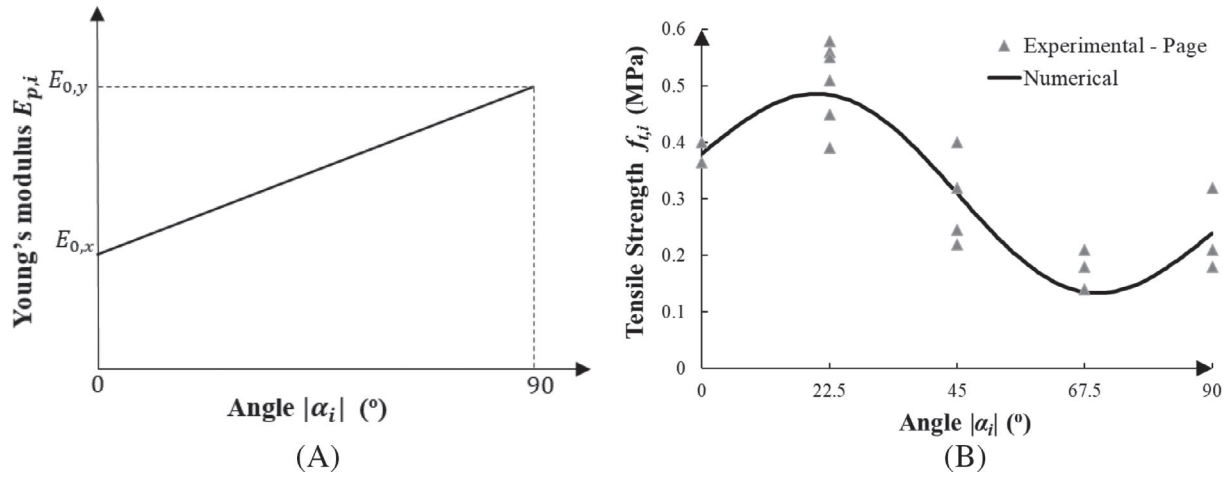


FIGURE 2 Variation of (A) Young's modulus E_i and (B) tensile strength $f_{t,i}$ along different directions α_i

Finally, once cracking occurs, the material properties are fixed. In essence, when cracking initiates in one of the two principal directions i , a new set of angles $\alpha_{crack,i}$ is defined and used in the following steps for the calculation of the material parameters; these are the angles inscribed by the principal tensile strains ε_i in the direction i and the direction parallel to the bed-joints at the onset of cracking. In the context of a TSRC model, the crack (and therefore also the crack plane) can still rotate (α_i changes), but the material properties will no longer change with this rotation (they are now calculated with $\alpha_{crack,i}$). This is a reasonable assumption, since a crack constitutes a weak plane, where future damage will probably localize and no stiffness or stress recovery will be expected.

2.2 | Tensile behavior

2.2.1 | Envelope curve for tension

Masonry exhibits brittle failure in tension. Most researchers describe the tensile behavior with two branches: a linear prepeak branch and a softening, postpeak branch, either linear or exponential. The softening rate is usually dependent on the fracture energy in tension, resulting in a more or less brittle failure depending on the value of the fracture energy.

In the current model, a linear ascending and a linear descending branch are used for the pre and postpeak behavior, respectively. However, a distinction is made on the postpeak behavior (softening rate) based on the cracking angle $\alpha_{crack,i}$. In the case of cracking angles in close proximity to 90° , horizontal cracks along the bed-joints are expected; this would correspond to bed-joint opening and in-plane flexural failure. Similarly, for $\alpha_{crack,i}$ close to 0° head-joint failure is expected. Finally, for angles around 45° diagonal cracking is expected, which is associated to diagonal shear cracking. The postpeak behavior is therefore related to the type of in-plane failure expected: brittle/flexural failure of bed- or head-joints exhibits higher softening rate, whereas diagonal shear failure exhibits a slower softening rate. To distinguish between the two different behaviors a threshold angle (θ_{fl}) is defined to mark the transition from flexural to shear failure (Figure 1B). It should be noted that the definitions of the cracking and threshold angles are based on the assumption that the shear failure shows a locally ductile frictional behavior, a condition that is typically obtained when the bricks are sufficiently strong and the mortar is relatively weak, resulting in cracks forming alongside the mortar joints. By observations of the crack patterns presented in Reference 40 for stretcher bond, reasonable values for the threshold angle could vary between 20 to 30° . Moreover, the brick pattern can give an indication of the angle of the expected diagonal crack and by considering a reasonable percentage of variation around it (in the case that some cracks might go through the bricks or skip a head joint and pass through the next), a threshold angle can be chosen. The tensile behavior is depicted in Figure 3A and is formulated as:

$$\sigma_i = \begin{cases} E_i \varepsilon_i & \text{for } \varepsilon_{cr,i} \geq \varepsilon_i \geq 0 \\ \max(f_{t,i}; \sigma_{un}) \left[1 - \frac{\varepsilon_i - \varepsilon_{cr,i}}{\varepsilon_{ult,i} - \varepsilon_{cr,i}} \right] & \text{for } \varepsilon_{ult,i} \geq \varepsilon_i \geq \varepsilon_{cr,i} \\ E_{res,i} \varepsilon_i & \text{for } \varepsilon_i > \varepsilon_{ult,i} \end{cases} \quad (8)$$

where

$$\varepsilon_{ult,i} = \begin{cases} \min \left\{ \frac{f_{t,i}}{\beta_i} + \varepsilon_{cr,i}; 100\varepsilon_{ult,k} \right\} & \text{for } \theta_{fl} \geq |\alpha_{crack,i}| \geq 0^\circ \\ 100\varepsilon_{ult,k} & \text{for } 90^\circ - \theta_{fl} > |\alpha_{crack,i}| > \theta_{fl} \\ \min \left\{ \frac{f_{t,i}}{\beta_i} + \varepsilon_{cr,i}; 100\varepsilon_{ult,k} \right\} & \text{for } 90^\circ \geq |\alpha_{crack,i}| \geq 90^\circ - \theta_{fl} \end{cases} \quad (9)$$

In the above equations $\varepsilon_{cr,i}$ are the cracking strains in direction i , given by $\varepsilon_{cr,i} = f_{t,i}/E_i$, whereas $\varepsilon_{ult,k}$ correspond to the ultimate strains along the global direction $k = x, y$, which are expressed as

$$\varepsilon_{ult,k} = \frac{2G_{ft,k}}{f_{t,k}h} \quad (10)$$

with $k = x$ when $i = 1$ and $k = y$ when $i = 2$, and h is the crack/crush bandwidth. The softening rate β_i is given by:

$$\beta_i = \begin{cases} \frac{\beta_x (|\alpha_{crack,i}| - \theta_{fl})^2}{\theta_{fl}^2} & \text{for } \theta_{fl} \geq |\alpha_{crack,i}| \geq 0^\circ \\ \beta_y \sin(4.5 (|\alpha_{crack,i}| - (90^\circ - \theta_{fl}))) & \text{for } 90^\circ \geq |\alpha_{crack,i}| \geq 90^\circ - \theta_{fl} \end{cases}, \quad (11)$$

where β_x and β_y are the softening rates for stresses parallel to the x and y directions and are given by:

$$\beta_k = \frac{f_{t,k}}{\varepsilon_{ult,k} - \frac{f_{t,k}}{E_k}} \quad (12)$$

Finally, σ_{un} is a stress value that resembles the shear capacity and it is given by Equation (13).

$$\sigma_{un} = \begin{cases} \max \{ \omega c_0 - \tan \phi (\sigma_{yy,0} + E_{0,y} \delta \varepsilon_{yy}); \omega c_0 \} & \text{for } 90^\circ - \theta_{fl} \geq |\alpha_{crack,i}| \geq \theta_{fl} \\ \omega c_0 & \text{else} \end{cases}, \quad (13)$$

where, $\sigma_{yy,0}$ is the stress normal to the bed joints at the beginning of the step, $\delta \varepsilon_{yy}$ is the incremental strain normal to the bed joint, and ω is a damage factor ranging from 0 and 1, with 0 and 1 referring to a fully cracked and uncracked integration point respectively. It is expressed as $\omega = \max(\omega_1, \omega_2)$, with

$$\omega_i = \min \left\{ 1; \max \left\{ 0; \frac{\varepsilon_{ult,i} - \varepsilon_i}{\varepsilon_{ult,i} - \varepsilon_{cr,i}} \right\} \right\}. \quad (14)$$

2.2.2 | Unloading/reloading behavior for tension

Even though no experiments exist for the cyclic behavior of masonry subjected to direct tension, from tests on walls it has been observed that the total dissipated energy is higher when the failure mode is governed by shear and smaller when it is governed by flexure.⁴¹ Based on this observation, a distinction is made on the unloading/reloading behavior of masonry subjected to tension, depending on the crack direction (flexural or shear crack). When diagonal shear failure is expected, i.e. for $\theta_{fl} \leq |\alpha_{crack,i}| \leq 90^\circ - \theta_{fl}$, bilinear unloading/reloading is adopted with elastic stiffness E_i until the critical stress limit $-\sigma_{un}$ (Equation (13)), which defines the second unloading/reloading branch (Figure 3A), is reached. This results in permanent deformations, as often observed in step-wise diagonal cracks. On the other hand, for angles outside this range, corresponding to in-plane flexural failure, secant unloading is adopted (Figure 3A).

2.3 | Compressive behavior

2.3.1 | Envelope curve for compression

The compressive behavior of masonry is described through three curves as formulated in Equation (15).

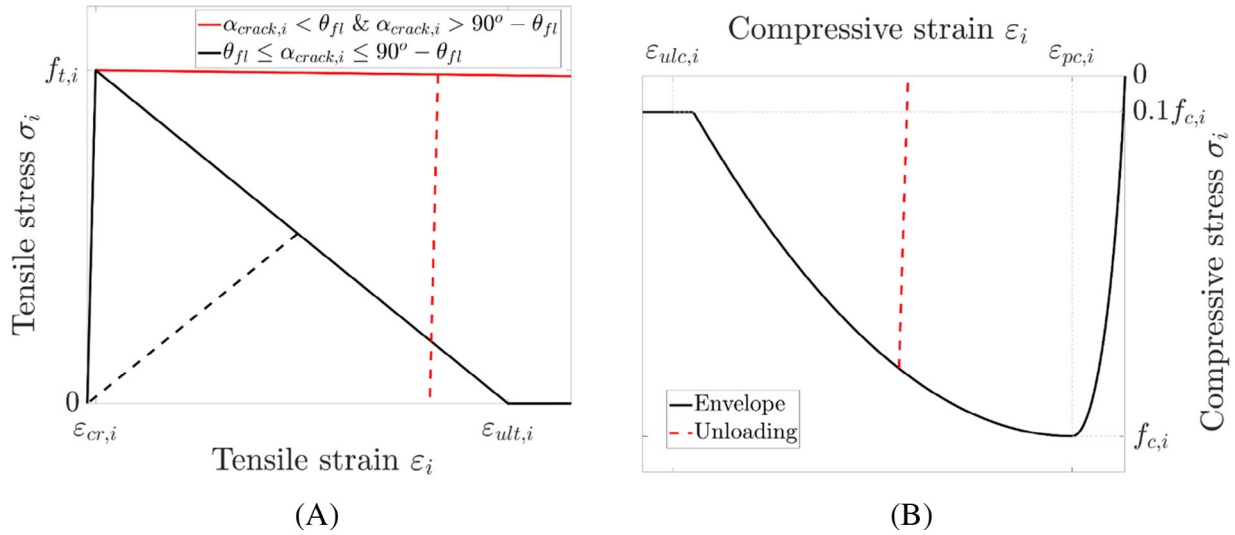


FIGURE 3 (A) Tensile behavior of masonry for the two different types of cracks: steep softening with secant unloading in case of flexural cracking ($\theta_{fl} > |\alpha_{crack,i}|$ and $90^\circ - \theta_{fl} < |\alpha_{crack,i}|$) and softening with elastic (linear) unloading in case of diagonal shear cracking ($\theta_{fl} \leq |\alpha_{crack,i}| \leq 90^\circ - \theta_{fl}$); (B) compressive behavior of masonry

$$\sigma_i = \begin{cases} E_i \varepsilon_i \left[1 - \frac{1}{n_i} \left(\frac{\varepsilon_i}{\varepsilon_{pc,i}} \right)^{n_i-1} \right] & \text{for } 0 > \varepsilon_i \geq \varepsilon_{pc,i} \\ \min \left\{ f_{c,i} \left[1 - \left(\frac{\varepsilon_i - \varepsilon_{pc,i}}{\varepsilon_{ulc,i} - \varepsilon_{pc,i}} \right)^2 \right]; 0.1f_{c,i} \right\} & \text{for } \varepsilon_{pc,i} > \varepsilon_i \geq \varepsilon_{ulc,i} \\ 0.1f_{c,i} & \text{for } \varepsilon_i < \varepsilon_{ulc,i} \end{cases} \quad (15)$$

where σ_i and ε_i are the stress and strain along the principal direction i , respectively, and $n_i = E_i / (E_i - E_{sec})$, with $E_{sec} = f_{c,i} / \varepsilon_{pc,i}$. Knowing that the area under the envelope is equal to $g_{fc,i} = G_{fc,i} / h$, where h is the crack/crush bandwidth that depends on the particular finite element configuration (e.g., References 42-45), inserted to achieve mesh-size objectivity. The ultimate strain in compression $\varepsilon_{ulc,i}$ is calculated as

$$\varepsilon_{ulc,i} = \min \left\{ \varepsilon_{pc,i} + \frac{3}{2f_{c,i}} \left(g_{fc,i} - E_i \left(0.5 - \frac{1}{n_i(n_i+1)} \right) \varepsilon_{pc,i}^2 \right); 1.2\varepsilon_{pc,i} \right\}. \quad (16)$$

For the prepeak curve the model proposed by Reference 46 for concrete is used, whereas for the postpeak curve a parabolic curve adopted from Reference 47 is selected. Finally, once the compressive fracture energy is consumed, a residual strength of $0.1f_{c,i}$ is adopted to avoid numerical instabilities. The envelope curve is depicted in Figure 3B.

2.3.2 | Unloading/reloading behavior for compression

Experimental research on the behavior of masonry subjected to cyclic compression⁴⁸⁻⁵² has shown that the material behaves nonlinearly, with accumulation of nonreversible strains and stiffness degradation. The unloading and reloading branches follow different paths and the reloading stiffness decreases with every new cycle during the postpeak response. Nevertheless, in this model no distinction is made between the unloading and reloading branch. Similar to unloading in tension for diagonal shear cracking, bilinear unloading is adopted with initial stiffness equal to the elastic Young's modulus E_i until the critical value σ_{un} is reached, which defines the upper limit of the second branch, as depicted in Figures 3B and 6. In the case of reloading, first, linear elastic stiffness is assumed until the lower limit $\sigma_{fc,i}$ (the stress that corresponds to the minimum compressive strain ever reached during the loading history) is reached, where ideal plastic behavior is adopted. This assumption differs from the cyclic behavior in pure compression. However, since the rotating principal behavior aims to capture indirectly also the shear behavior, the elastic unloading/reloading branch turns out to

better represent the overall cyclic behavior, which is of crucial importance in the global hysteretic behavior of masonry walls. This will be explained further in Section 2.5 and in the description of the validation examples (Section 3).

2.3.3 | Reduction of compressive strength with lateral cracking

Similar to concrete, it is assumed that tensile cracks parallel to a compressive strut reduce the compressive strength capacity of that strut.^{19,53} The presented model adopts the reduction model proposed by Reference 54 for concrete. Hence, the compressive strength is reduced after cracking as:

$$f_{c,i} = \min \left\{ \frac{1}{1 + K_{c,i}} f_{c,i}; 0.1 f_{c,i} \right\}, \quad (17)$$

where

$$K_{c,i} = \min \left\{ 0.27 \left(\frac{\alpha_{t,j}}{|\epsilon_{pc,i}|} - 0.37 \right); 1 \right\} \geq 0 \quad (18)$$

with $\alpha_{t,j}$ representing the maximum tensile strain reached during the loading history in the direction j perpendicular to i . To simplify, for $i = 1, j = 2$ and for $i = 2, j = 1$. At the same time, no increase in the compressive strength due to biaxial compression is considered, i.e., tension-compression behavior is accounted for but biaxial compression is not.

2.4 | Indirect inclusion of shear behavior

Many authors have investigated the shear behavior of masonry and concluded that the shear capacity of brick masonry subjected to confinement/compression can be described by Coulomb friction.^{34,40,55} Some have also highlighted the importance of dilatancy.^{56,57} In damage mechanics and plasticity models, the shear capacity is introduced through the damage or yield surfaces, respectively. However, in smeared crack models there are different ways to describe shear. In fixed smeared crack models the shear capacity along the plane of the fixed crack is explicitly taken into account via a shear retention factor (or function) along that crack plane. Although shear retention can describe aggregate interlock in concrete, it may lead to stress-locking when the crack bands propagate through the mesh in a zig-zag manner⁵⁸. Rotating smeared crack models describe the behavior in the continuously rotating principal direction and, hence, do not explicitly describe shear. However, an implicit shear term is required to guarantee coaxiality between principal stresses and strains.¹⁹ For masonry, the shear behavior along the bed-joints is important and should be considered in the description of the constitutive equations. Ignoring the shear behavior of masonry may lead to overestimation of the structure's base shear capacity (e.g. Reference 18).

This model introduces the shear capacity via an internal iterative process that ensures that the shear stress τ_{xy} does not exceed the shear capacity τ_{\max} ($|\tau_{xy}| \leq \tau_{\max}$). This process is indirect: the shear stress τ_{xy} is not described through a total stress-strain relationship. Instead, only the shear stress in the direction of the mortar-joints (which coincide with the global x-y-directions) is limited based on a Coulomb-friction criterion. In order to do so, first the stresses in the global x- and y-coordinates ($\sigma_{xx}, \sigma_{yy}, \tau_{xy}$) are calculated through Equation (19). Once the global stresses are known, the shear capacity τ_{\max} is derived according to Equation (21). If the absolute value of the shear stress ($|\tau_{xy}|$) is lower than τ_{\max} no further action is required; the shear strength computed at the integration point is sufficient to withstand the shear stress τ_{xy} . However, if $|\tau_{xy}|$ exceeds the shear capacity, shear sliding occurs and the shear stress needs to be limited to $|\tau'_{xy}| = \tau_{\max}$. The new global stress σ'_{xx} is calculated via Equation (22), with the assumptions that the vertical confinement level (σ_{yy}) does not change, and that coaxiality between principal stresses and strains is maintained. A graphical representation through Mohr's circle is given in Figure 4.

$$\begin{Bmatrix} \sigma_{xx} \\ \sigma_{yy} \\ \tau_{xy} \end{Bmatrix} = [T_{\sigma}]^{-1} \begin{Bmatrix} \sigma_1 \\ \sigma_2 \\ 0 \end{Bmatrix} \quad (19)$$

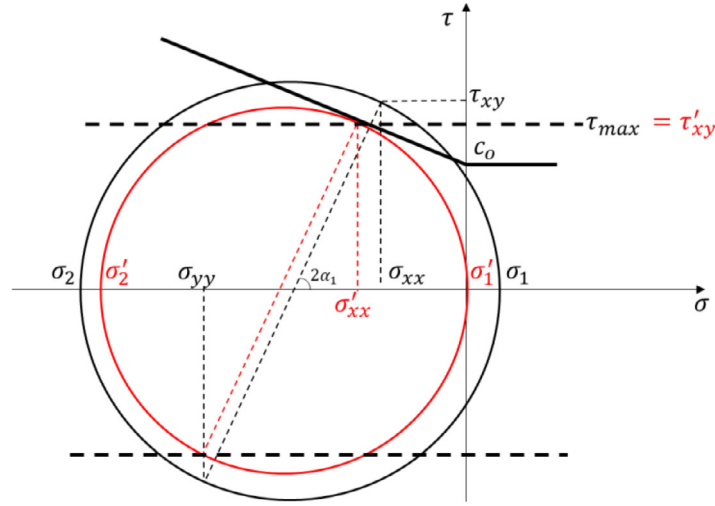


FIGURE 4 Representation of Mohr circle and recalculation of shear stress τ'_{xy} , normal stress (σ'_{xx}) and principal stresses (σ'_1, σ'_2) in the case of shear failure $|\tau_{xy}| > \tau_{max}$

with

$$[T_\sigma]^{-1} = \begin{bmatrix} \cos^2 \alpha_1 & \sin^2 \alpha_1 & -2 \cos \alpha_1 \sin \alpha_1 \\ \sin^2 \alpha_1 & \cos^2 \alpha_1 & 2 \cos \alpha_1 \sin \alpha_1 \\ \cos \alpha_1 \sin \alpha_1 & -\cos \alpha_1 \sin \alpha_1 & \cos^2 \alpha_1 - \sin^2 \alpha_1 \end{bmatrix}, \quad (20)$$

$$\tau_{max} = \max \{c_0 - \sigma_{yy} \tan \phi; c_0\}, \quad (21)$$

$$\tan 2\alpha_1 = \frac{2 |\tau'_{xy}|}{\sigma'_{xx} - \sigma_{yy}}. \quad (22)$$

Consequently, due to the new set of global stresses ($\sigma'_{xx}, \sigma_{yy}, \tau'_{xy}$), the principal stresses (σ'_1, σ'_2) across the directions α_i need to be recalculated, with the inverse procedure of Equation (19). If the new principal stresses (σ'_1, σ'_2) are within the limits set by the envelope for the corresponding principal strains, the shear calculation is completed. However, in the case that one or both of them exceed their corresponding limit, they need to be further reduced. These limits are given by the following equation:

$$\begin{aligned} -\sigma_{un} &\leq \sigma'_i \leq \sigma_{f,i} & \text{if } \varepsilon_i \geq 0 \\ \sigma_{f,i} &\leq \sigma'_i \leq \sigma_{un} & \text{if } \varepsilon_i < 0 \end{aligned} \quad (23)$$

,where $\sigma_{f,i}$ and $\sigma_{f,c,i}$ are the stresses that correspond to the maximum and minimum strain ε_i ever reached during the loading history of the integration point, whereas σ_{un} is the stress value defined in Equation (13). The calculation of the new principal stresses is followed by the reevaluation of the global stresses and the check of the shear capacity anew. This procedure is repeated until either all the above mentioned conditions are met or, in the case the conditions cannot be satisfied simultaneously, until a maximum number of 500 iterations is reached. In the latter case, priority is given in maintaining coaxiality and satisfying the criteria of Equation (23), resulting therefore in a final shear stress τ_{xy} that may still exceed the shear capacity. The number of maximum iterations was selected after performing a sensitivity study between 50, 100, and 500 iterations, as the latter resulted in the most satisfactory numerical results in terms of numerical stability and damage localization without compromising significantly the computational time. For a graphical representation, one can refer to the flowchart of Figure 5. Please note that x and y refer to the directions parallel to bed- and head-joint, respectively; so the model, though it formulates the behavior in the rotating principal directions, assesses the shear capacity along the predefined joint directions. In other words, the model does not check the shear stresses along the principal directions (their value being null by definition) or in the direction corresponding to the crack initiation (as in existing fixed-crack

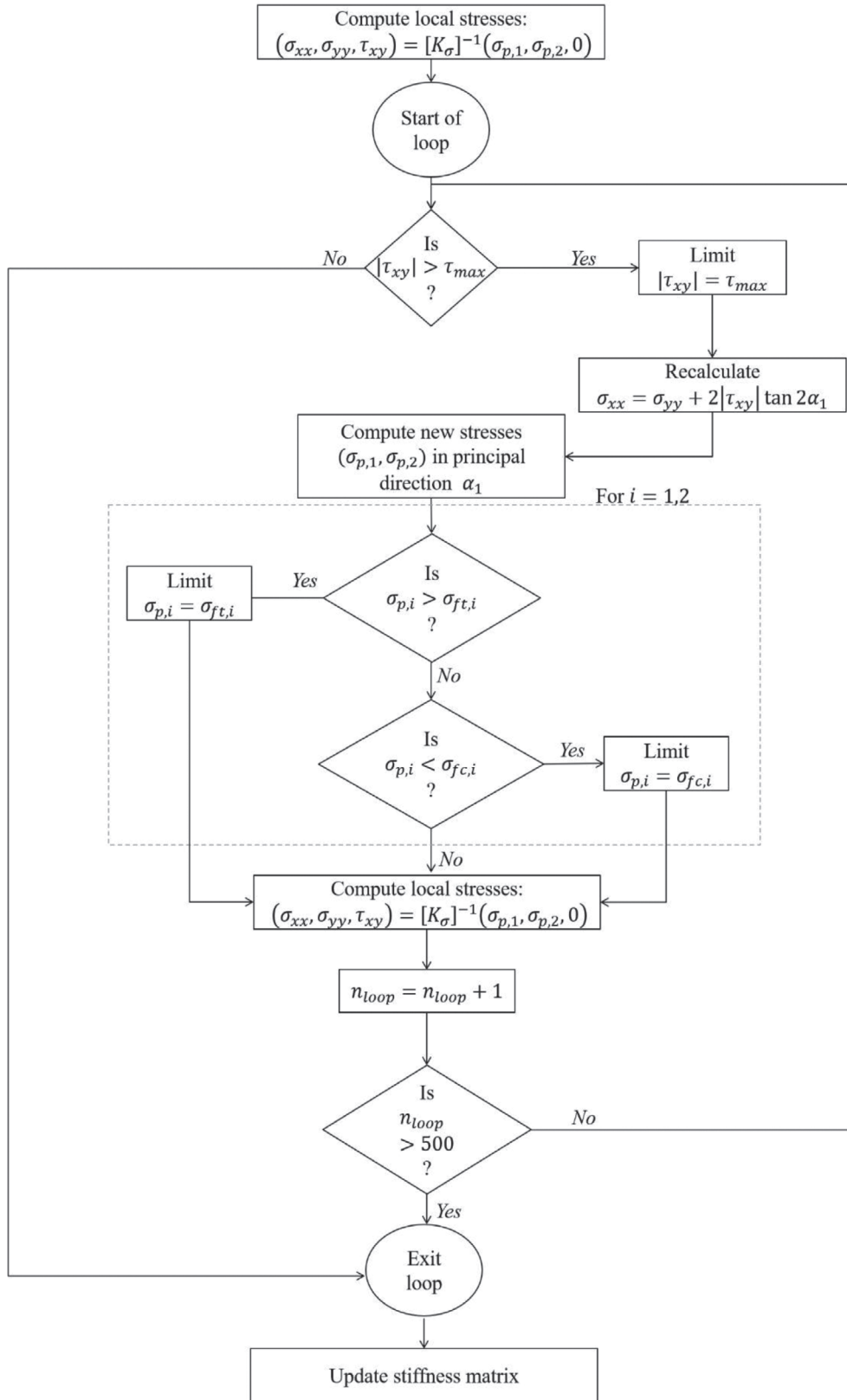


FIGURE 5 Flowchart of internal iterative loop for shear stress limitation

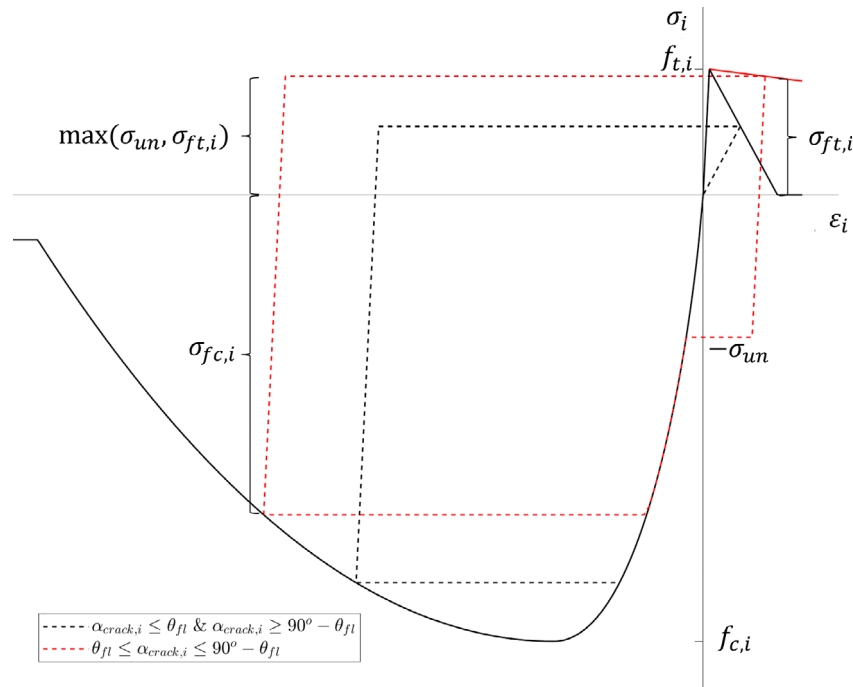


FIGURE 6 Cyclic behavior of masonry as adopted in the presented model. The dashed red lines refer to the unloading when shear cracks are expected, whereas the dashed black lines refer to unloading when flexural cracks are expected. Here it is assumed that the σ_{un} is constant (which means that the vertical compressive stress σ_{yy} remains constant)

models), but it rather limits the value of the shear stresses in the predefined x - y (bed joint/head-joint) directions, based on a Coulomb friction formulation. This addresses the specific characteristics of masonry as compared to concrete.

2.5 | Overall cyclic behavior

As mentioned before, linear unloading with elastic stiffness E_i is adopted in compression. In tension two unloading/reloading possibilities are included in the model: when the cracking angle corresponds to a diagonal crack ($90^\circ - \theta_{fl} \geq |\alpha_{crack,i}| \geq \theta_{fl}$), the unloading/reloading behavior in tension is assumed to be elastic (linear); when the cracking angle relates to a flexural crack, secant unloading/reloading is adopted. Moreover, an upper and lower limit are set when unloading (or reloading) from compression (to tension) and from tension (to compression), respectively. This is the limit σ_{un} which was defined already in Equation (13). In contrast to damage and fracture models, which generally adopt secant unloading and reloading, and often underestimate the dissipated energy, this model allows to increase the dissipated energy, especially when failure is governed by shear. A depiction of the integrated cyclic behavior for compression and tension, including the two options for the types of tensile cracks, is presented in Figure 6.

3 | VALIDATION

In order to assess the applicability and validity of the developed constitutive model, the constitutive equations were inserted in a FORTRAN subroutine and subsequently implemented in the finite element software DIANA FEA, version 10.4. Four walls, tested in the past under cyclic in-plane loading, are modeled; each one differs from the others either in aspect ratio, axial load, boundary conditions or material properties. Two of the modeled walls were tested under cyclic quasi-static conditions at the Joint Research Centre of the European Community in Ispra; these double-wythe walls comprised solid clay bricks and had an aspect ratio of 2 (high wall referred as HIGSTA here) and 1.35 (low wall referred as LOWSTA here).^{59,60} The vertical precompression level was 0.6 MPa. The remaining two walls, named TUD-COMP-4 and TUD-COMP-6, were built and tested at Delft University of Technology in 2015⁴¹; they were both single-wythe calcium silicate (CS) brick walls with a low aspect ratio of 0.7, and a vertical precompression of 0.5 MPa. Also the boundary

TABLE 1 Geometrical properties and failure mechanisms of the in-plane wall experiments used for validation

Specimen name	Dimensions	Vertical precompression		
	$l_w \cdot h_w \cdot t_w$ [m]	[MPa]	Boundary condition	Failure mechanism
LOWSTA	1.0 · 1.35 · 0.250	0.60	Double clamped	Diagonal shear
HIGSTA	1.0 · 2.0 · 0.250	0.60	Double clamped	Flexure/rocking
TUD-COMP-4	4.0 · 2.76 · 0.102	0.50	Double clamped	Diagonal shear
TUD-COMP-6	4.0 · 2.76 · 0.102	0.50	Cantilever	Diagonal shear + crushing

TABLE 2 Masonry material properties adopted for the continuum numerical models (for the LOWSTA and HIGSTA walls, the corrected values of joint cohesion and friction coefficient, as calculated in Reference 60, are used); unknown and thus assumed material properties are represented in italics, while the other properties were based on the companion material tests

Material properties used in the numerical analyses	TUD-COMP-4 & TUD-COMP-6			LOWSTA & HIGSTA		
			Horizontal direction $i = x$	Vertical direction $i = y$	Horizontal direction $i = x$	Vertical direction $i = y$
Modulus of elasticity	E_i	[MPa]	3583	5091	1491	<i>1491</i>
Shear modulus	G	[MPa]	1571		500	
Threshold angle	θ_{fl}	[°]	20		20	
Tensile strength	$f_{t,i}$	[MPa]	0.21	0.14	<i>0.1</i>	0.04
Compressive strength	$f_{c,i}$	[MPa]	7.55	5.93	6.20	<i>6.20</i>
Compressive strain at peak strength	$\varepsilon_{pc,i}$	[-]	<i>0.01</i>	<i>0.01</i>	<i>0.01</i>	<i>0.01</i>
Fracture energy tension	$G_{ft,i}$	[N/mm]	<i>0.02</i>	<i>0.012</i>	<i>0.01</i>	<i>0.005</i>
Fracture energy in compression	$G_{fc,i}$	[N/mm]	43.4	31.3	<i>40.0</i>	<i>40.0</i>
Cohesion	c_0	[MPa]	0.14		0.17	
Friction coefficient	$\tan \phi$	[-]	0.43		0.43	

conditions at the top varied amongst these benchmark tests; the two Ispra-walls and TUD-COMP-4 were clamped at top and bottom (double clamped), while TUD-COMP-6 was clamped only at the bottom (cantilever). However, for all the walls the top side was allowed to move vertically so that the precompression level would remain constant. The walls exhibited different failure mechanisms: in-plane flexural failure (rocking), diagonal shear failure, and a combination of diagonal shear failure and crushing/splitting. The geometrical properties and failure mechanisms of the walls are presented in Table 1.

The material properties adopted are presented in Table 2. These properties were obtained by companion material tests that were carried out at the same time period and from the same batch of materials as the large wall tests.^{41,61,62} For some properties no data from companion tests was available. In that case, representative values were chosen based on literature. Specifically, this related to the fracture energies in tension, where values between 0.005 and 0.02 N/mm were chosen based on the formula $G_{ft,i} = 0.025(2f_{t,i})^{0.7}$. Moreover, for walls LOWSTA and HIGSTA, the same Young's modulus and compressive strength were adopted in both directions, and a reduced tensile strength was applied perpendicular to the bed joints. Finally, the threshold angle θ_{fl} was set to 20°.

All of the presented numerical models adopted 3 × 3 Gaussian integrated 8-noded quadratic, quadrilateral plane-stress elements with average dimensions of 100 mm × 100 mm. The Quasi-Newton (Secant) method was selected as the incremental-iterative solution procedure, and either the force or the displacement convergence norm needed to be satisfied, with a tolerance of 0.01. The analyses were permitted to continue in case the convergence criteria were not satisfied, in which case the relevance of the numerical results was examined.

Table 3 gives a comparison between the experimental and numerical results in terms of base shear capacity and corresponding displacement at peak, residual shear capacity and its corresponding displacement postpeak, that is, softening degradation, and energy dissipation for the four walls. The comparison of these key characteristics is subsequently elaborated and discussed in Sections 3.1–3.4.

TABLE 3 Base shear capacity F_{peak} and its corresponding displacement at peak δ_{peak} , residual base shear F_{res} at the ultimate displacement and total dissipated energy U for the experimental and numerical results of the modeled walls

Walls	Experimental				Numerical			
	F_{peak} [kN]	δ_{peak} [mm]	F_{res} [kN]	U [10^2 kN mm]	F_{peak} [kN]	δ_{peak} [mm]	F_{res} [kN]	U [10^2 kN mm]
LOWSTA	+81.0	+2.8	+48.4	22.9	+78.2	+2.9	+67.6	20.4
	-83.7	-2.7	-59.0		-78.8	-2.8	-61.2	
HIGSTA	+71.7	+12.5	+67.8	12.9	+77.3	+8.2	+75.0	22.5
	-71.9	-12.0	-71.0		-78.4	-9.1	-74.6	
TUD-COMP-4	+119.1	+2.6	+97.6	55.1	+118.6	+0.9	+70.0	20.6
	-123.4	-0.3	-108.5		-116.2	-1.4	-93.0	
TUD-COMP-6	+109.8	+4.3	+68.1	187.4	+101.5	+1.6	+53.5	157.5
	-109.0	-4.2	-65.6		-104.1	-2.3	-56.1	

3.1 | Low wall specimen LOWSTA

The low wall LOWSTA was a double clamped wall, with an aspect ratio of 1.35 and a precompression load of 0.6 MPa. It exhibited brittle failure with diagonal shear cracking. The maximum experimental base shear was 81 kN, whereas the minimum base shear was -83.7 kN. After diagonal cracking, the residual postpeak base shear was measured to be 48.4 kN (-40% reduction) and -59 kN (-57% reduction) for the positive and negative loading direction respectively.

The numerical strength capacity was estimated to be 78.2 kN (3.5% underestimation) and -78.8 kN (5.8% underestimation). The residual postpeak strength of this wall was overestimated with the current numerical model: the remaining strength capacity was 67.6 kN in the positive and -61.2 kN in the negative direction, overestimating the experimental residual base shear by 39% and 3%, respectively. The hysteresis response obtained from the numerical analysis well reproduces the experimental curve (Figure 7A). Small dissipation is observed in the prepeak phase, for top displacements up to 1.5 mm, whereas the increased energy dissipation is clearly visible for the postpeak cycles. The agreement with the experiment is attributed to the inclusion of energy dissipation in the material model through the bilinear unloading/reloading for compression and tension (when shear cracks form). The dissipated energy (area inscribed by the force-displacement hysteretic loops) of the numerical model was 10.7% smaller than the experimental one (Table 3), but this is within reasonable accuracy. A model with fully secant unloading/reloading would miss this aspect. As already mentioned, the cyclic behavior of masonry has not received much attention and many constitutive models for masonry have only been tested for

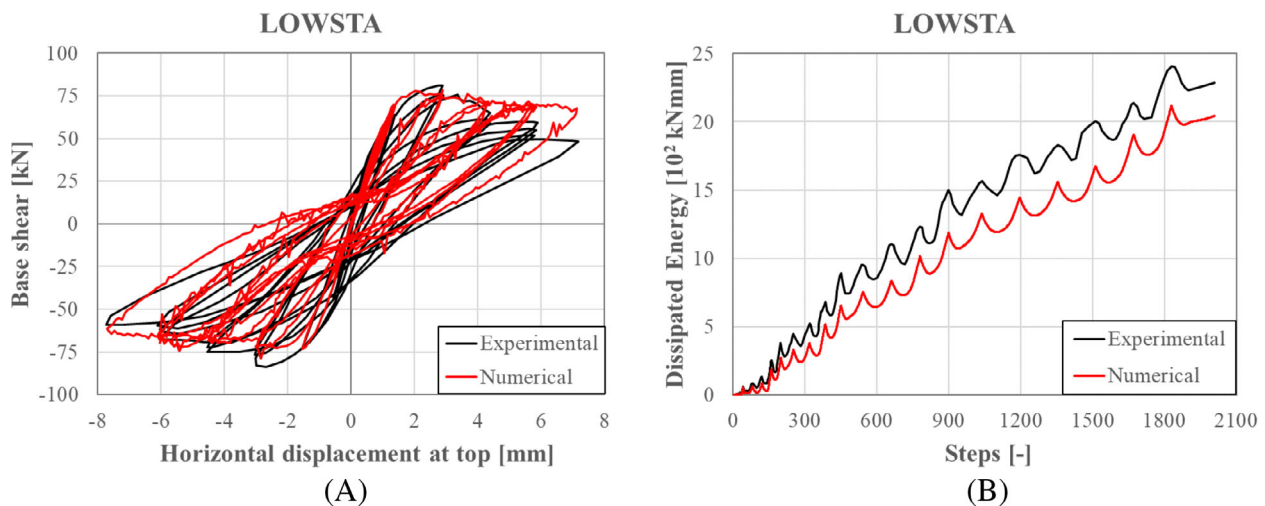


FIGURE 7 Comparison of (A) experimental crack pattern, and (B) maximum tensile strain ever reached during the loading history, depicted at the end of the numerical analysis, for the wall LOWSTA

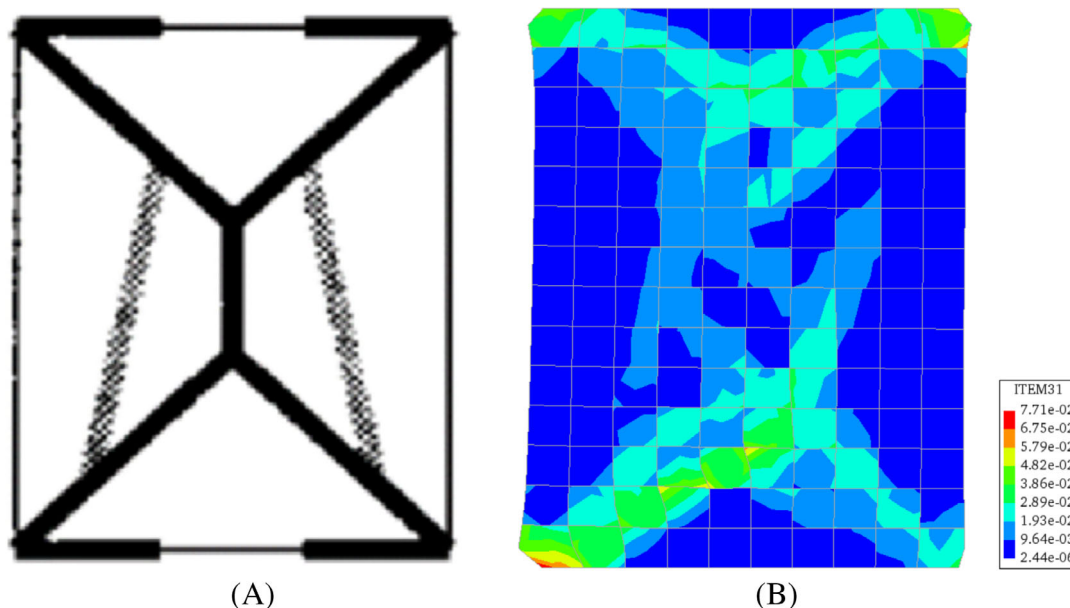


FIGURE 8 Comparison of experimental (black) and numerical (red) results of (A) hysteretic response (base shear vs. displacement) and (B) energy dissipation of shear wall LOWSTA

monotonic loading. The numerical curves show some small oscillatory irregularities, which are related to local temporary loss of convergence, as will be explained in Section 4.1.

The damage localization of the numerical model and the experiment were in agreement, with both of them showing initially horizontal cracks at the corners, and diagonal cracks extending from the corners towards the center of the wall, where they intersected. Subsequently, the two sets of diagonal cracks were connected by a vertical crack (or a slightly inclined crack in the case of the numerical model) (Figure 8). A difference was observed regarding the angle of cracks between the experiment and the numerical model. However, this is to be expected in a macromodel, where the brick pattern is not described and where the mesh size and orientation can influence the results. In this research a fixed size (100 mm × 100 mm) and order (3 × 3) of mesh was chosen for all examined walls, which may be considered rather coarse for this particular wall. A small study on mesh sensitivity regarding the order and size of mesh will be discussed in Section 4.3.

3.2 | High wall specimen HIGSTA

The high wall HIGSTA had an aspect ratio of 2 and a precompression load of 0.6 MPa. It exhibited flexural behavior with rocking and minimal strength degradation. The maximum and minimum experimental base shear were 71.7 and −71.9 kN, respectively. The residual postpeak base shear was only 3.4% and 0.9% smaller than the maximum base shear in the positive and negative direction, respectively.

The numerical model overestimated the base shear capacity, with a maximum capacity of 77.3 kN (7.6% overestimation) and a minimum of −78.4 kN (9% overestimation). This is the only numerical model that overestimated the corresponding experimental capacity. Similarly to the experiment, minimal softening was observed with residual values of 75 and −76.4 kN. Again, the model appears to be able to reproduce properly the cyclic behavior, as compared to other models that either start from secant or elastic unloading/reloading curves (e.g., Reference 18). The energy dissipation in the early cycles is close to that of the experiment, while for the last two repetitions an overestimation was observed. The total energy dissipation (Table 3 and Figure 9B) was overestimated, with the majority of the energy (61%) being released during the last two repetitions. However, the overestimation of the capacity and energy dissipation can be considered within acceptable limits. The overestimation of the energy dissipation was likely caused by the small diagonal shear cracks that developed during the last two loading cycles and their corresponding state of compressive and tensile stresses.

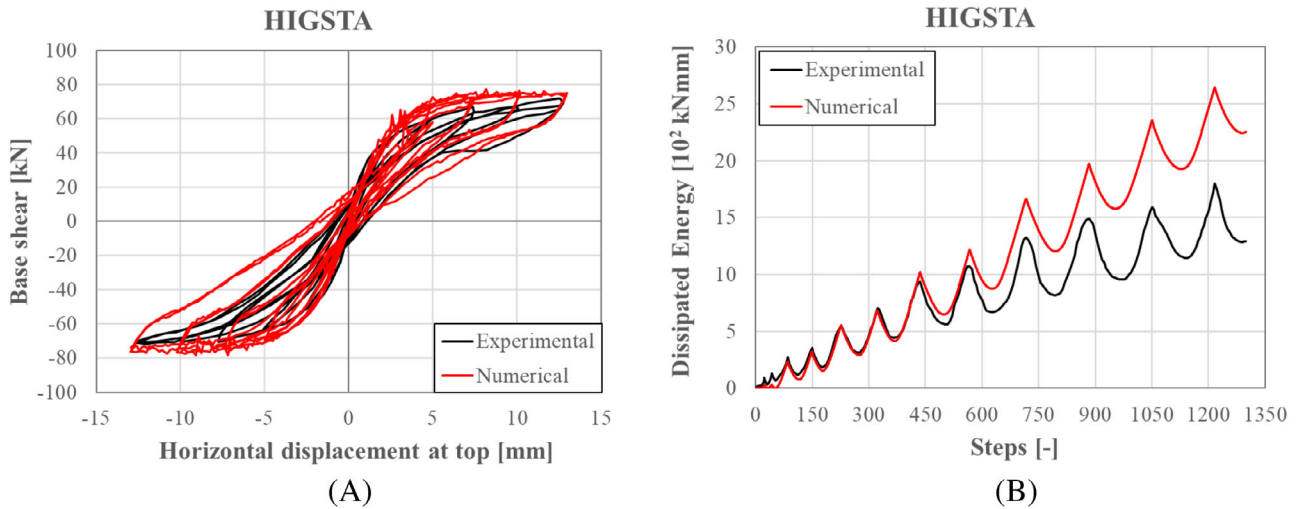


FIGURE 9 Comparison of (A) experimental crack pattern, and (B) maximum tensile strain ever reached during the loading history, depicted at the end of the numerical analysis, for the wall HIGSTA

The failure mechanism was rocking, with flexural cracks forming at the top and bottom layers of the wall, both for the experiment and the numerical model (Figure 10). In the case of the numerical model, it seems that some diagonal cracks also started forming at the top and bottom towards the center of the wall. This was not reported after the particular quasi-static experiment. Nevertheless, when the wall was tested again for a higher precompression load of 0.8 MPa, diagonal cracks also formed in the experiment, extending from the corners towards the center of the wall.⁵⁹ This indicates that the occurrence of the diagonal cracking mode is close to the occurrence of crack/crush rocking mode, especially when the precompression load increases. In that case softening and higher energy dissipation is observed post-peak as the energy consumption for local constitutive shear and compression cycles is much higher than for tension cycles.

3.3 | Squat wall TUD-COMP-4

Specimen TUD-COMP-4 was a double-clamped squat calcium-silicate brick wall (aspect ratio of 0.7) with a vertical pre-compression load of 0.5 MPa. Brittle shear failure was observed, with diagonal cracks running through the mortar joints approximately along the diagonal of the wall, initially formed at the center of the wall and then expanding towards the corners. In the positive direction the maximum shear force was 119.1 kN; in the negative direction the minimum shear force is slightly higher and equal to -123.4 kN. The wall reached an ultimate displacement of 5.39 mm (0.2% drift) in the positive and -5.35 mm (-0.19% drift) in the negative loading direction at the corresponding shear capacities of 97.6 kN (-18% postpeak reduction) and -108.5 kN (-12% postpeak reduction), respectively. Due to the pure shear failure a large amount of energy was dissipated.

The numerical model estimated the force capacity of the wall with good accuracy, predicting a maximum of 118.6 kN (-0.36% with respect to experimental) and a minimum of -116.2 kN (-5.8% with respect to the experimental value) (Figure 11A and Table 3). The numerical softening rate was higher than the experimental and more softening occurred in the positive loading direction, with a lowest value of 70 kN (41% reduction of capacity and 28.2% underestimation of experimental value) and -93 kN (19.9% reduction of numerical capacity and 14.2% underestimation of experimental value). This asymmetry in the softening rate could be due to the accumulation of damage and the reduction of the compressive capacity due to lateral cracking, and also due to the indirect shear limitation. The numerical model underestimates significantly (-63.7%) the dissipated energy. (Figure 11B). This may be due to the fact that in the experiment pure shear failure occurred with an almost fully elastic unloading/reloading behavior, while in the numerical model a combination of shear-compression failure occurred, affecting the energy consumption in the final cycles.

Regarding the damage localization, the crack pattern of Figure 12 is compared to the maximum tensile strain ever reached during the loading history of the wall in Figure 13. The similarities in the pattern are apparent: diagonal cracks

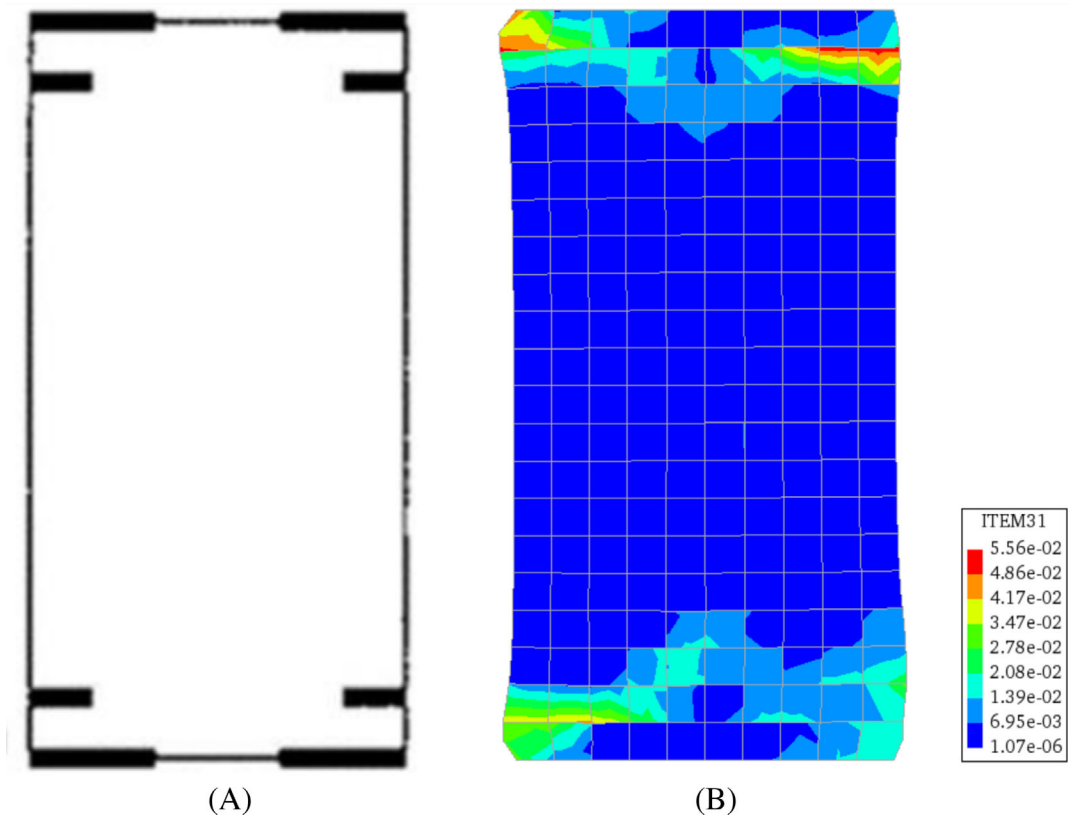


FIGURE 10 Comparison of experimental (black) and numerical (red) results of (A) hysteretic response (base shear vs. displacement) and (B) energy dissipation of slender wall HIGSTA

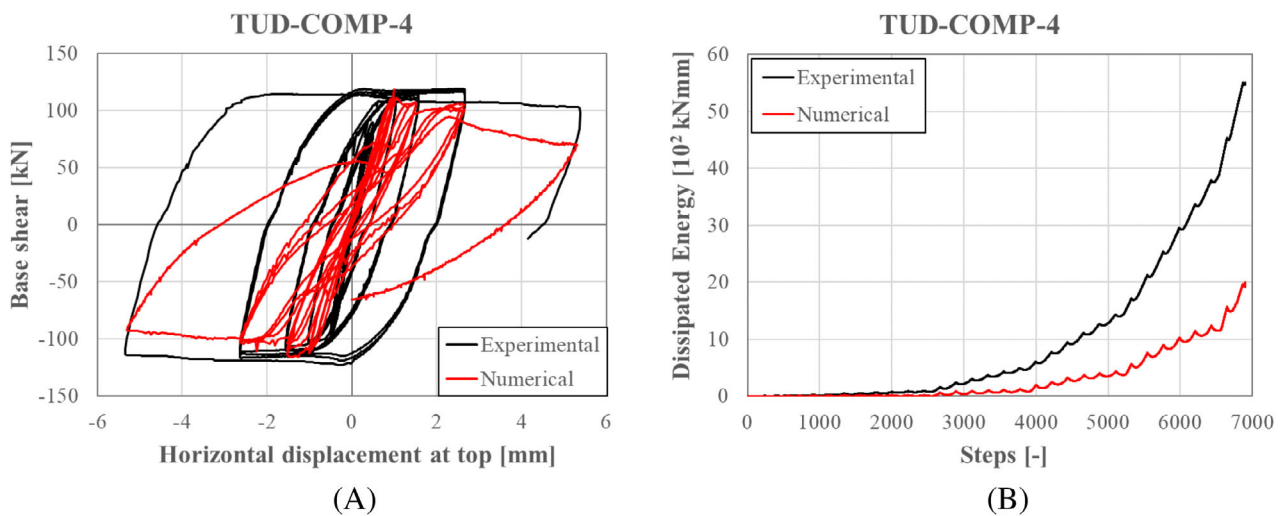


FIGURE 11 Comparison of experimental (black) and numerical (red) results of (A) hysteretic response (base shear vs. displacement) and (B) energy dissipation of squat wall TUD-COMP-4

running from the corners of the walls towards the center were observed in both cases. In the case of the numerical analysis, the orientation of the cracks in the center was smaller than in the corners but not zero, whereas in the experiment a horizontal crack was present instead. The two main numerical cracks are asymmetric. This is partially due to the different material properties for the involved integration points (depending on the angle of strains at the onset of cracking), but also due to the recalculation and limitation of the stresses because of the indirect shear limitation. Nevertheless, the very

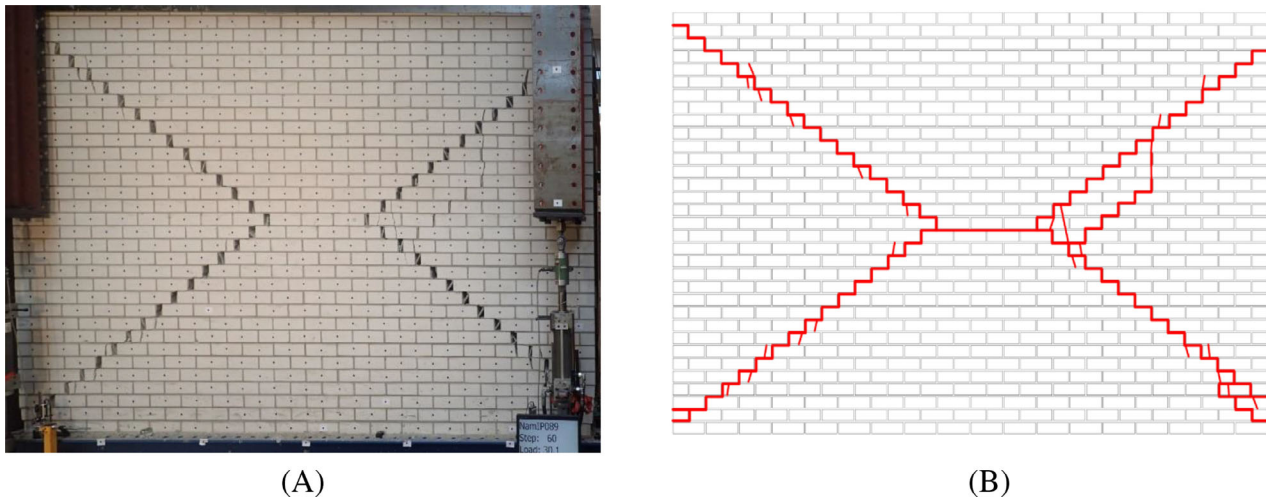


FIGURE 12 Wall component TUD-COMP-4 (A) accumulated damage and crack at the end of the experiment, (B) crack pattern observed at the end of the experiment

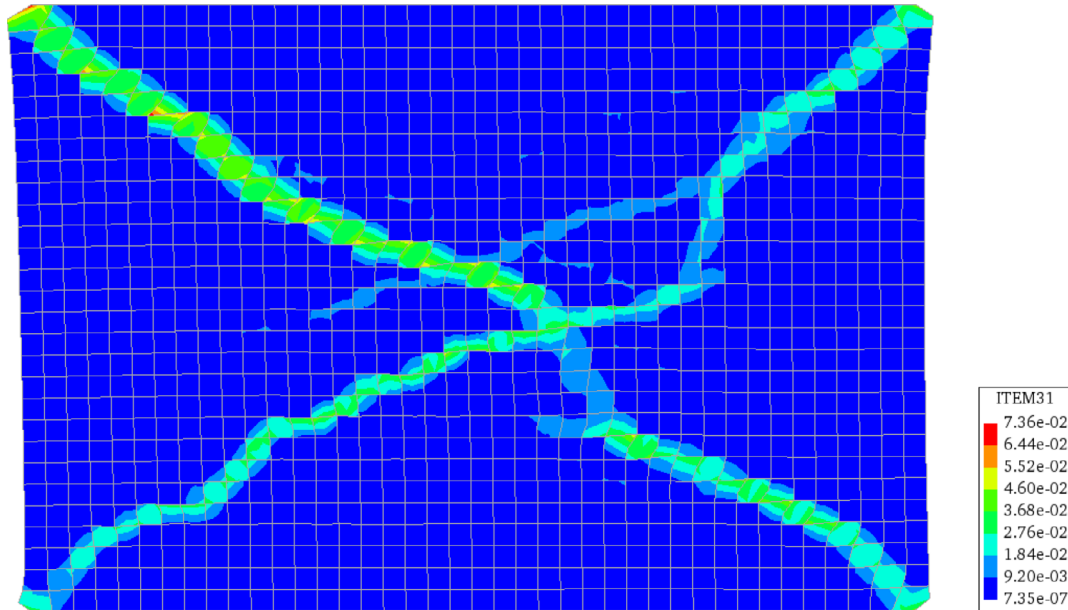


FIGURE 13 Maximum tensile strain ever reached during the loading history of wall TUD-COMP-4, depicted at the end of the numerical analysis

localized damage well replicates the experimental outcome. This ability of the model to predict localized patterns, while predicting the correct base shear capacity, is an improvement compared to other existing continuum models that may show too distributed crack patterns (e.g., References 18, 24).

3.4 | Squat wall TUD-COMP-6

Wall TUD-COMP-6 was a cantilever squat calcium-silicate brick wall (aspect ratio 0.7, same as TUD-COMP-4), with a precompression load of 0.5 MPa. The maximum and minimum experimental force capacities were 109.8 kN and -109 kN respectively. The wall exhibited brittle shear failure, with cracks running through the wall diagonally. Two to three parallel step-wise cracks can be observed in Figure 14 for each loading direction. Moreover, brick splitting prevailed at the

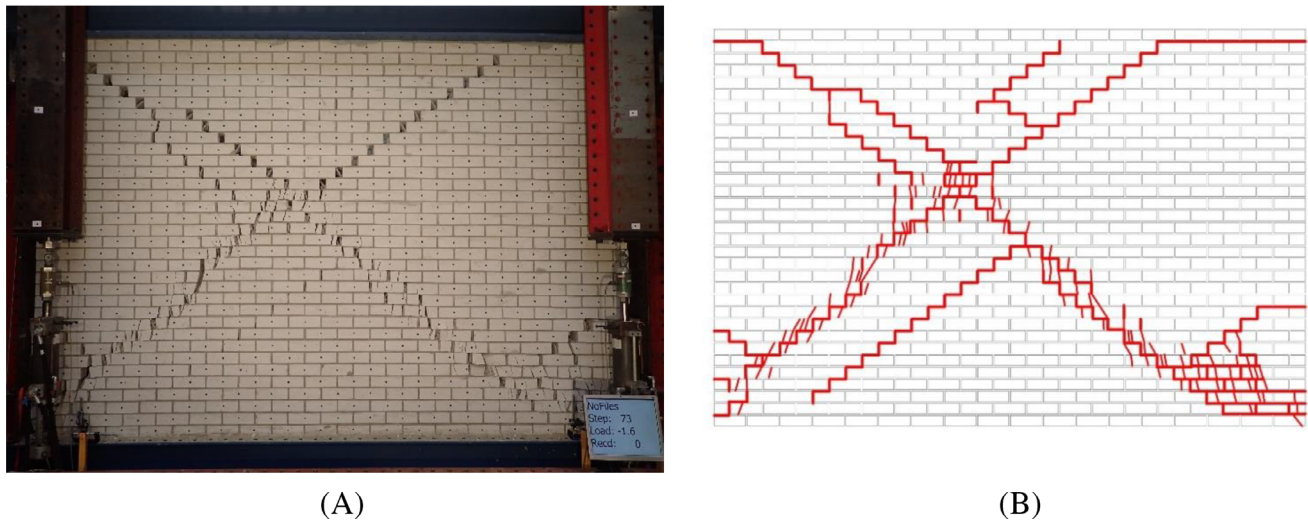


FIGURE 14 Wall component TUD-COMP-6 (A) accumulated damage and crack at the end of the experiment, (B) crack pattern observed at the end of the experiment

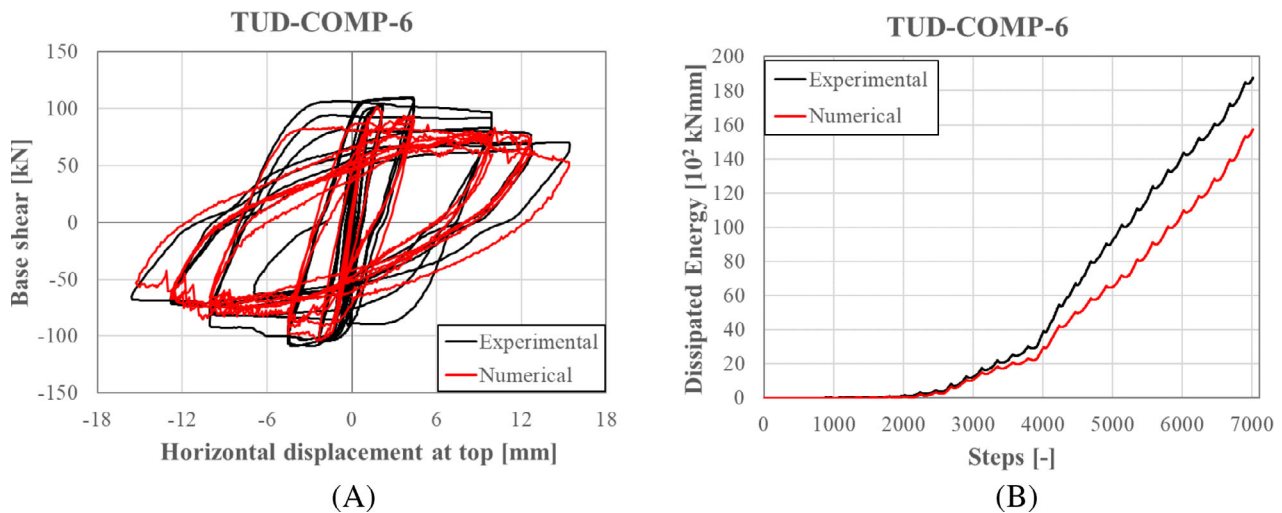


FIGURE 15 Comparison of experimental (black) and numerical (red) results of (A) hysteretic response (base shear vs. displacement) and (B) energy dissipation of squat wall TUD-COMP-6

center and at the toes of the wall. The force capacity gradually reduced with every new cycle, with a final value of 68.1 kN for an ultimate displacement of 15.4 mm in the positive direction, and a value of -65.6 kN at a displacement of -15.6 mm.

The numerical model slightly underestimated the force capacity, with a maximum of 101.5 kN (-7.6% with respect to the experimental) and a minimum of -104.1 kN (-4.5%). Similar to component TUD-COMP-4, the peak force capacity was reached in earlier loading cycles and more strength degradation was observed for the numerical model than the experimental (Figure 15A and Table 3). The maximum and minimum numerical force capacities corresponding to the maximum and minimum drifts were 53.5 kN (-21.5% underestimation) and -56.1 kN (-14.4% underestimation), while the total dissipated energy was 17.4% lower than the experimental. In this case, the simultaneous occurrence of diagonal shear cracks with crushing/splitting of the bricks, both in the experimental and numerical results, resulted in a bigger degradation of the unloading/reloading stiffness during the last three loading cycles. This is well-depicted in the numerical results both in terms of stiffness and strength degradation and energy dissipation, as seen in Figure 15.

Comparing Figures 14 and 16, one can see the similarities in the damage localization. In both cases diagonal cracks were prevailing, a few were parallel to each other and some wider than others. Even though the maximum tensile strains of the numerical model (Figure 16) did not follow exactly the same direction as in the experiment, the general crack pattern

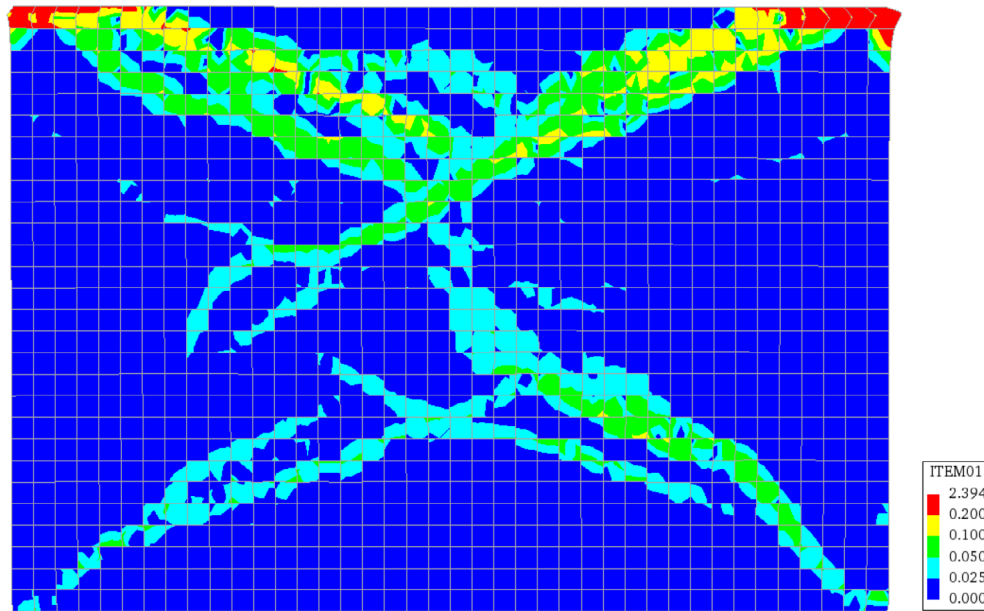


FIGURE 16 Maximum tensile strain ever reached during the loading history of wall TUD-COMP-6, depicted at the end of the numerical analysis

was well depicted; even the horizontal sliding along the two horizontal cracks at the top left and right of the wall was represented in the numerical results (red localization zone in Figure 16). Similar to wall TUD-COMP-4, some asymmetry is observed in the crack pattern. Apart from the reasons already mentioned for wall TUD-COMP-4, an additional factor that contributed to the asymmetry observed in this wall is the asymmetrically applied external displacement, which was slightly higher when loading in the negative direction.

4 | DISCUSSION

The comparison between the experimental results and the corresponding numerical predictions shows that the developed constitutive model estimates with good accuracy the base shear capacity of in-plane loaded masonry walls. Additionally, it predicts the correct failure mode and leads to very localized cracks, representative of those observed in the experiments (although the cracks do not perfectly match and their orientation can slightly differ). Compared to other existing macromodels that use implicit solution procedures the damage localization has improved, since it concentrates along few “lines” of elements and is not distributed over many elements, as has been observed in the past (e.g., References 16, 20, 63). Also in terms of cyclicality, the model seems to perform better than models that assume fully secant or fully elastic unloading/reloading. The dissipated energy is best estimated in the cases that a combination of failure mechanisms occurs. Specifically, for walls LOWSTA and TUD-COMP-6 underestimation of 10%–17% is observed, which could be considered within acceptable limits for macromodels, but for wall TUD-COMP-4 the underestimation is much bigger. On the other hand, the model overestimated the dissipated energy of HIGSTA. It appears that the numerical estimation is closer to the experimental results when a combination of different failure mechanisms is observed (flexure and shear for LOWSTA, and shear and crushing for TUD-COMP-6), whereas when only one mechanism is observed during the experiment (flexure for HIGSTA and pure shear for TUD-COMP-4) the model still predicts some hybrid mechanism and then is incapable of predicting the precise value. In the case of HIGSTA, the shear cracks that started developing in the numerical model dissipated more energy than the pure rocking cracks of the experiment. As for walls TUD-COMP-4 and TUD-COMP-6, during the experiment a major part of the energy was dissipated due to the shear sliding behavior. Even though the developed model incorporates the ductile energy-absorbing unloading/reloading behavior in shear, this is limited for cracks with initial orientation between 20–70°; if a crack forms originally due to flexure, it will always have a brittle behavior with secant unloading and small energy dissipation when unloading/reloading in tension.

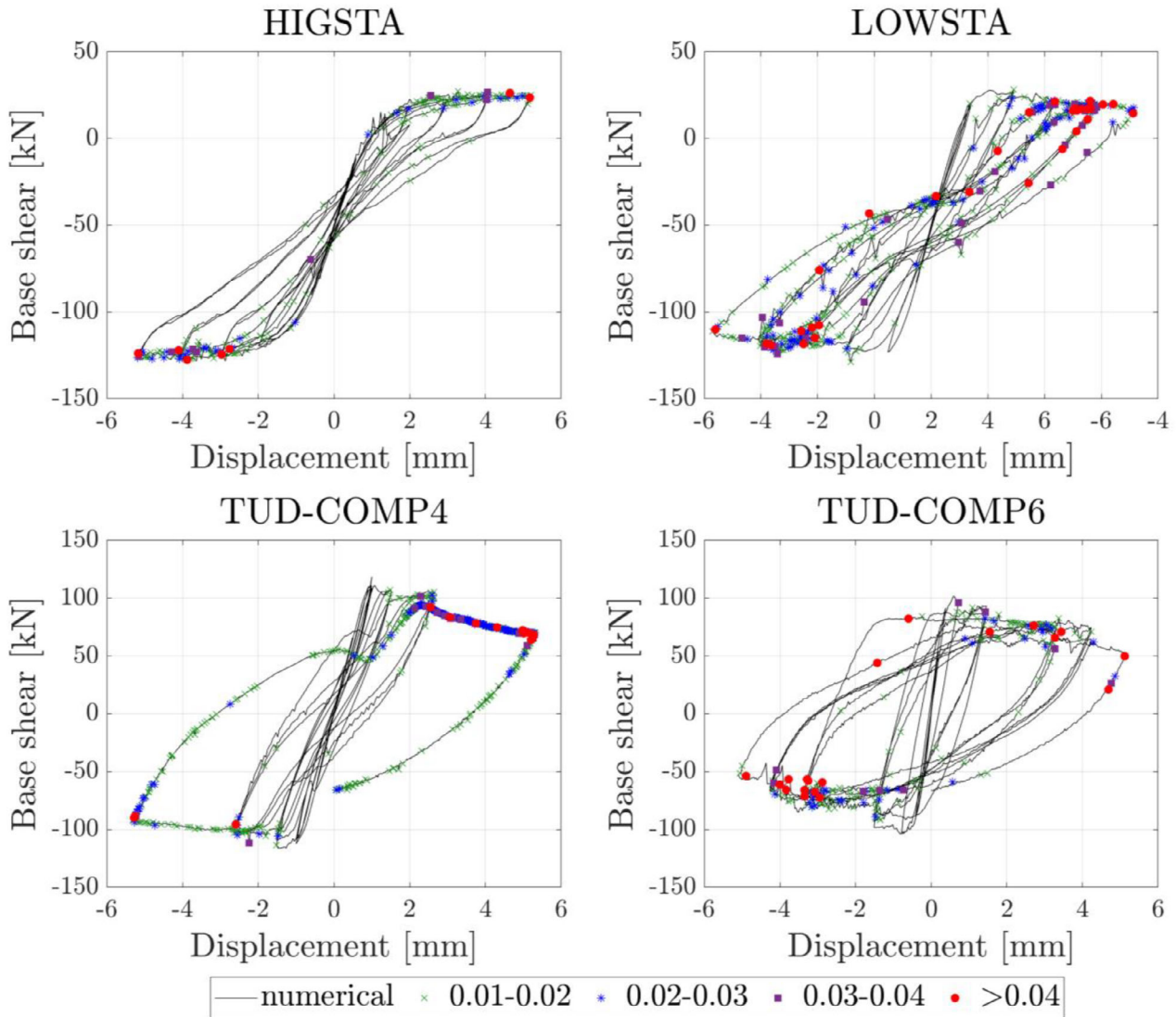
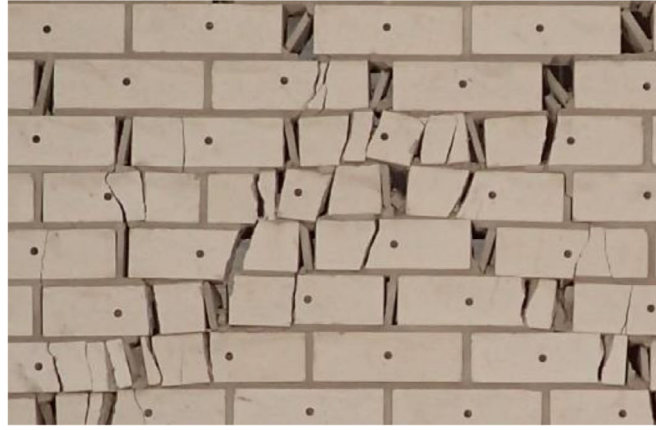


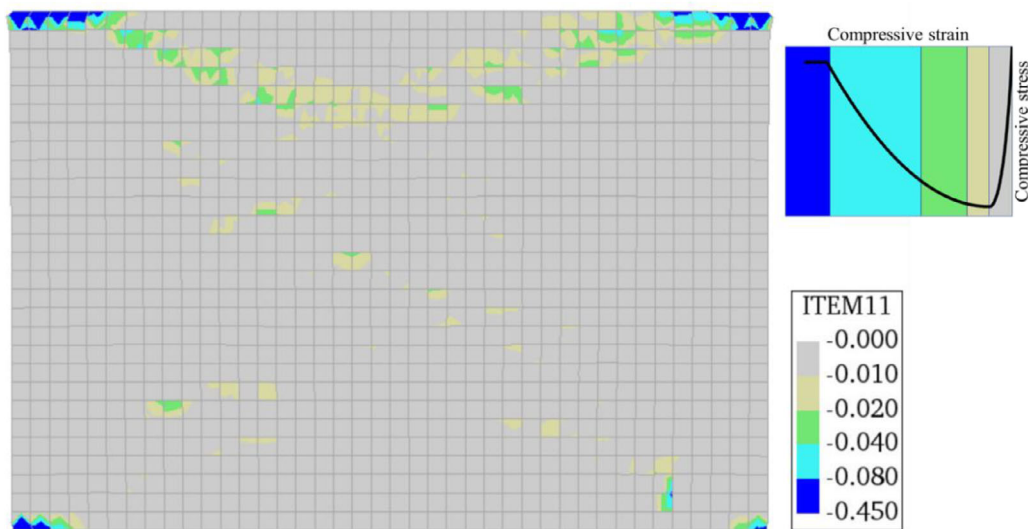
FIGURE 17 Location of unconverged steps on the force-displacement curve and the range of their convergence norm for the modeled walls HIGSTA, LOWSTA, TUD-COMP-4, and TUD-COMP-6

4.1 | Numerical stability and convergence

Figure 17 presents the force-displacement curve and the steps that did not converge for each numerical analysis. The maximum number of iterations was set to 100 with a convergence tolerance of 0.01 for both displacement and force norms, and, in the case that convergence was not satisfied, the analysis was permitted to continue to the next step (it is reminded that for convergence either the force or the displacement norm need to be satisfied). The range of the convergence norm is depicted in different colors. Figure 17 shows therefore not only the number and location of the unconverged steps, but also the error in the tolerance, to allow for an easier assessment of the accuracy of the numerical results. Some of the spikes and oscillations observed in the force-displacement curve coincide with steps where convergence was not reached, whereas other spikes did not relate with stability issues. Moreover, there are even some points that would not rise suspicion of instability, but did not converge momentarily. For three out of the four walls many steps did not reach convergence, but convergence was reached in the following steps. This was not the case for wall TUD-COMP-4, for which none of the steps on the softening branch converged during the loading in the positive direction of the last cycle. For most of these steps the norm was lower than 0.03, and the force-displacement curve does not show evident signs of such numerical instabilities (such as spikes or sudden drops of capacity).



(A)



(B)

FIGURE 18 (A) detail of crushing (split bricks and mortar joints) at the center of wall TUD-COMP-6, (B) minimum compressive strain ever reached during the loading history of TUD-COMP-6, depicted at the end of the numerical analysis (scale factor 1)

In general, between 1.5% (TUD-COMP-6) to 7.8% (LOWSTA) of the total number of steps for each analysis had a convergence norm higher than 0.02. These numerical instabilities are probably caused by the internal iterative algorithm defined to limit the shear strength. As a matter of fact, the recalculation of the principal stresses when the shear stress exceeds the shear strength can lead to significant changes in the stiffness matrix of the integration point, which consequently creates numerical instabilities in the Newton–Raphson procedure. This issue will be further investigated in future research.

4.2 | Compression nonlinearity of squat wall TUD-COMP-6

During the test performed on specimen TUD-COMP-6, reduction of the force capacity and high energy dissipation were observed due to compression nonlinearity. This compression nonlinearity physically emerged in the form of crushing of the mortar joints and splitting of the calcium-silicate bricks. This is illustrated in Figures 14B and 18A, where splitting of the bricks and crumbling of the mortar joints is observed both at the center of the wall (where the compressive struts meet) and alongside the compressive struts towards the bottom corners, with most of the crushing and splitting observed at the bottom right corner. To examine if the developed model captures adequately this compression

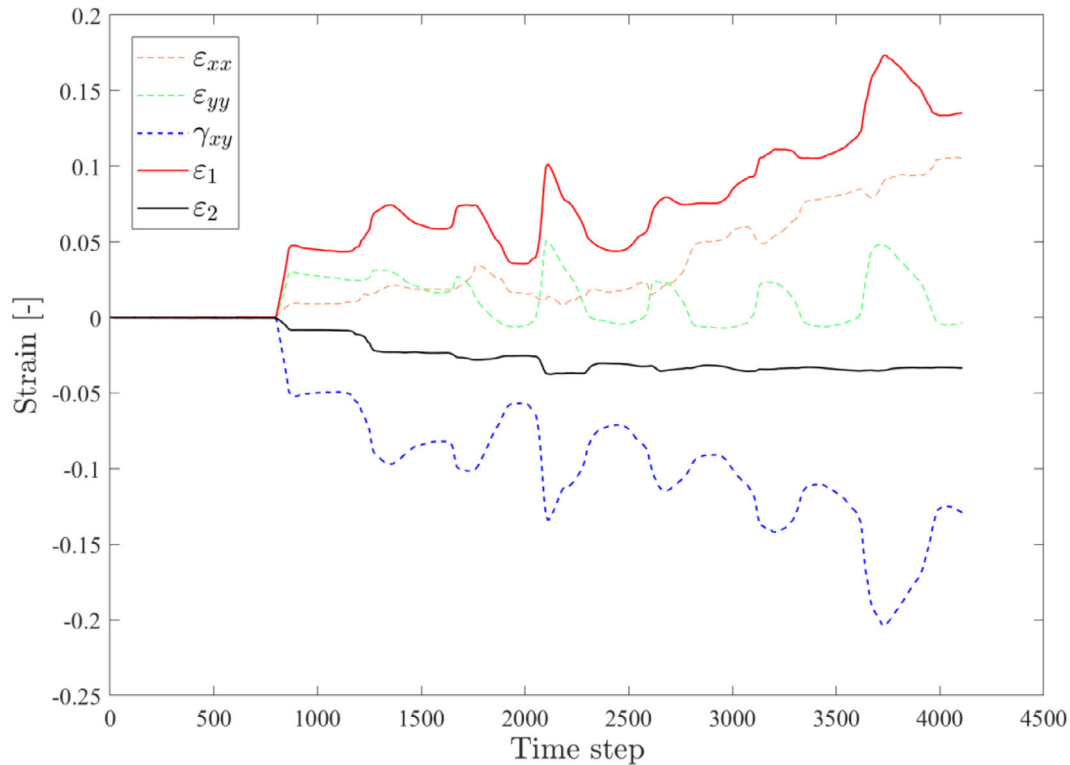


FIGURE 19 Evolution of strains (ϵ_{xx} , ϵ_{yy} , γ_{xy}) in global directions (x,y) and principal strains (ϵ_1 , ϵ_2) at the top right corner of wall TUD-COMP-6 through its loading history

nonlinearity (cracking and crushing) of masonry, a user status ($\alpha_{c,i}$) is defined and set equal to the minimum compressive strain ever reached during the loading history. If the value is smaller than the compressive strain corresponding to the peak strength, crushing/splitting has occurred.

In the numerical model, as seen in Figure 18B, crushing occurred in the elements along the compressive-shear strut, but most of it was concentrated at the top of the wall, with only six elements being crushed at the bottom two corners. The crushing of the top elements would not normally be expected in a cantilever wall and it wasn't observed in the experiment either. Lower compressive normal stresses are expected at the bottom of the wall and one would expect that crushing would first appear there. The top side of the wall was free to rotate and move vertically, but the strong bond to the steel beam (modeled as infinitely rigid in the numerical model) forced the top face of the wall to have the same horizontal displacements. In the case of the numerical model, the crushing observed at the top of the wall is due to the combination of two different factors. First, the lower (in absolute terms) normal compressive stresses σ_{yy} at the top of the wall led to a lower shear capacity τ_{max} . Due to the assumption of coaxiality and maintenance of σ_{yy} , the values of σ_1 and σ_2 are recalculated and there is the chance that the compressive principal stress reduces (in absolute value/increases in relative value) before reaching the peak strength. Lower strength resistance leads then to higher deformations. Secondly, even though the minimum ever reached compressive strain is smaller than the compressive strain related to crushing, a major part of the strain is attributed to the shear deformation (γ_{xy}) and not only to the normal deformations (ϵ_{xx} , ϵ_{yy}), as seen in Figure 19.

It is therefore recommended to check the stress and strain components both in the principal and global directions, to be able to distinguish if crushing is triggered by the internal shear limitation (and should be therefore ignored) or if it is due to compressive failure. For failure due to flexure or shear, no additional check is required.

4.3 | Mesh sensitivity

Another problem often encountered in standard strain-softening continua is their potential in objectivity with respect to the mesh size, mesh order and/or mesh direction. Many researchers tackle this sensitivity by including a mesh-adjusted

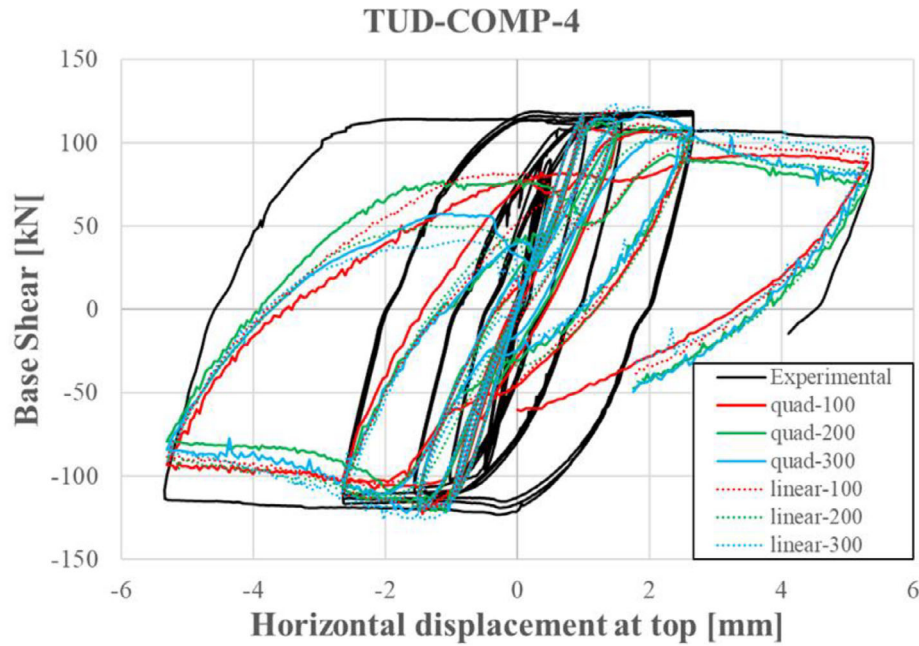


FIGURE 20 Base shear versus horizontal displacement at top for different mesh element size (100, 200, 300 mm) and order (quad for quadratic vs. linear)

softening modulus: the crack bandwidth or characteristic length.^{42-44,58,64} In this work, the crack bandwidth is estimated based on the element area A as: $h_{crack} = \sqrt{A}$ for quadratic elements and $h_{crack} = \sqrt{2A}$ for linear elements.⁵⁸ In order to test the sensitivity of the developed model on the mesh size and order, wall TUD-COMP-4 was modeled with elements of different order (quadratic 3×3 vs. linear 2×2) and different size (100, 200, 300 mm). Note that all the analyses were carried out using the same material properties, solution procedure and convergence criteria as for the model described in Section 3. However, only one repetition per cycle was applied.

The force-displacement curve and the damage localization (in terms of $\alpha_{i,1}$) are presented for the different models in Figures 20 and 21, respectively. All the models estimated the base shear capacity with good accuracy, with a maximum deviation of 5.2% between numerical and experimental capacity, and 9% between the maximum and minimum numerical capacity. Bigger deviations were observed in the postpeak behavior, where the models with quadratic elements exhibited more softening than those with linear elements. Overall, a maximum difference of 28.7% was observed in the residual strength between the numerical models, with the linear-300 element and quadratic-200 element exhibiting the minimum and maximum softening, respectively. In terms of crack pattern, all models predicted shear failure with diagonal cracks, but the crack angle and the point of intersection between the two diagonal cracks differed. Increasing the element size and/or order (quad-200, linear-200, linear-300) resulted in steeper crack angles. This could be attributed to the coarser mesh that offers less options for the direction of a diagonal crack. Note that a difference is observed in the crack localization of the wall for the reference elements (quad-100) from the analysis of Section 3, probably due to the fewer repetitions during the loading procedure and therefore smaller accumulation of permanent deformations.

4.4 | Threshold angle sensitivity

Finally, a small variation of the model was made to investigate how the threshold angle θ_{fl} , which defines the transition between flexural and shear behavior, influences the global behavior of the walls. Two threshold angles were selected: $\theta_{fl} = 20^\circ$ which leads to shear behavior for cracking angles between $20-70^\circ$ (original model), and an angle $\theta_{fl} = 25^\circ$ for which shear behavior is adopted for cracking angles between $25-65^\circ$. Wall TUD-COMP-4 was modeled with the two different variations and the results are presented in Figures 22 and 23. Both models predicted the base shear capacity with good accuracy (less than 5% difference) and only minor differences are observed in the postpeak behavior during the last

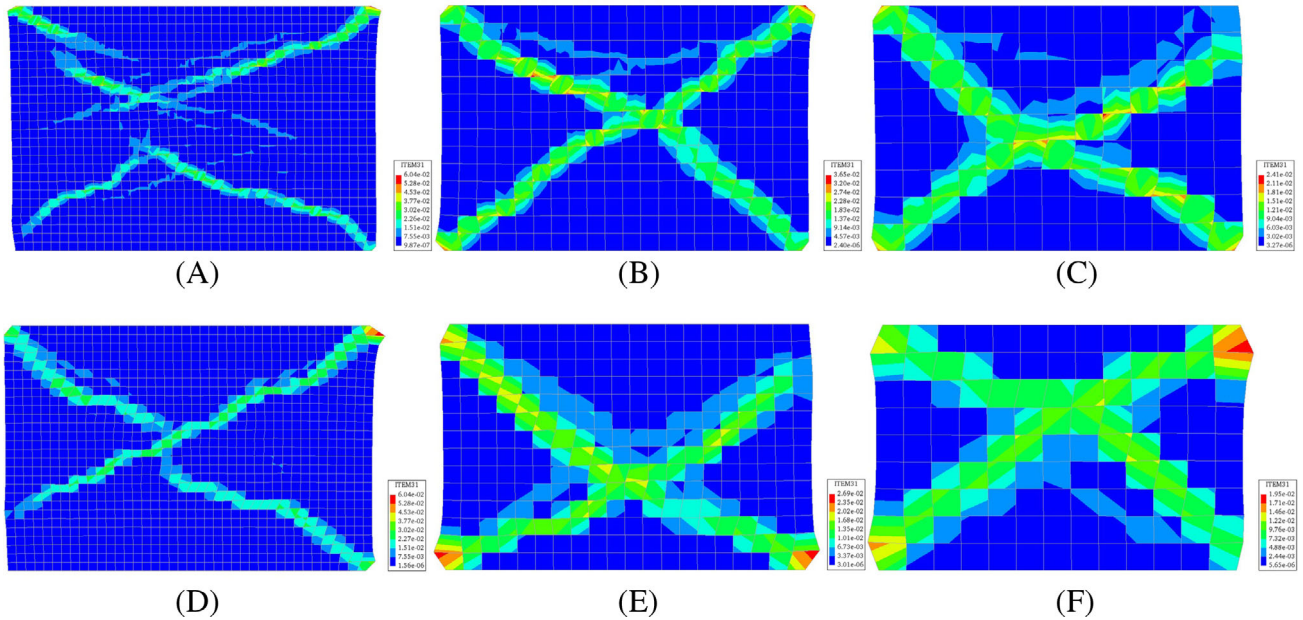


FIGURE 21 Comparison of maximum tensile strains ever reached during the loading history of wall TUD-COMP-4 in the case of (A) quadratic elements of 100 mm, (B) quadratic elements of 200 mm, (C) quadratic elements of 300 mm, (D) linear elements of 100 mm, (E) linear elements of 200 mm, and (F) linear elements of 300 mm

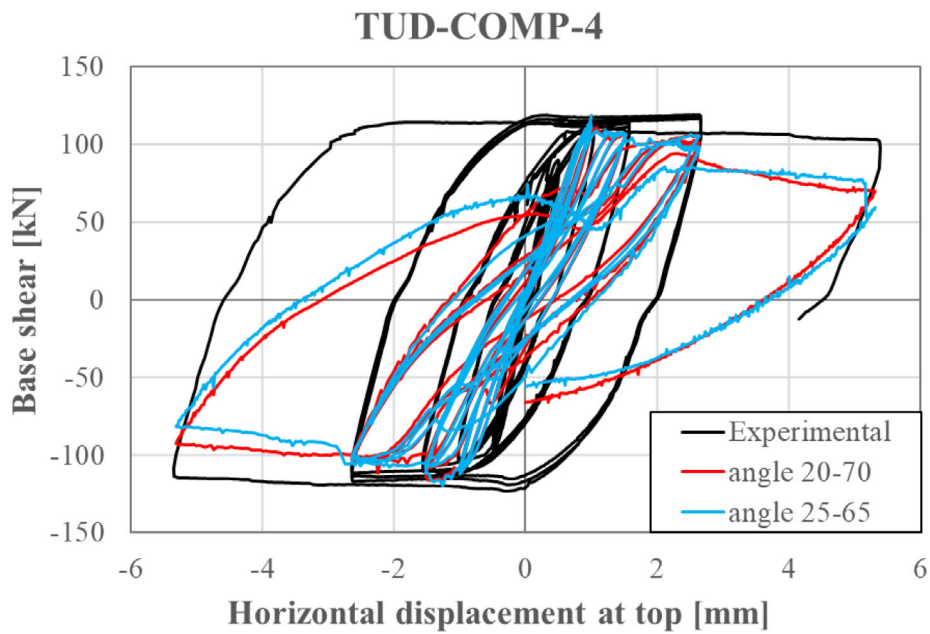


FIGURE 22 Influence of range of cracking angles associated with shear behavior and failure

cycle. On the other hand, the two analyses return different final crack patterns; although both models present diagonal shear cracks, a wider range of “shear angles” (20–70°) leads to steeper angles, more representative of the experiment. Therefore, the choice of a threshold value of 20° (and an angle range of 20–70°) is considered more appropriate for modeling long shear walls. For walls LOWSTA and HIGSTA, no difference in the numerical results (force-displacement and crack localization) was observed. This proves that these walls, with smaller aspect ratio, were not influenced by a difference of $\pm 5^\circ$ since flexure was predominant (for HIGSTA) and/or shear cracks were steeper (LOWSTA). Finally, for wall TUD-COMP-6 observations similar to those for TUD-COMP-4 were made.

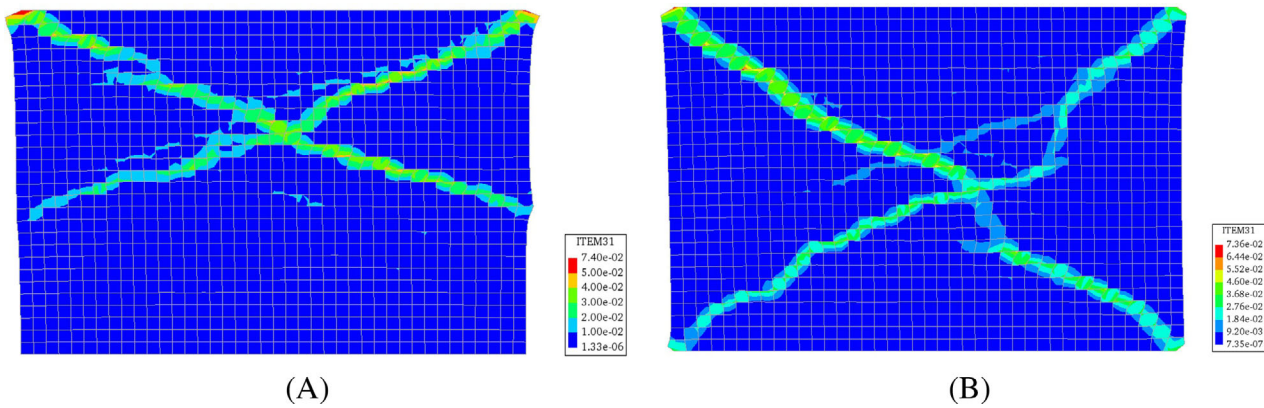


FIGURE 23 Comparison of maximum tensile strains ever reached during the loading history of wall TUD-COMP-4 when shear behavior is adopted for cracking angles between (A) 25–65° and (B) 20–70°

The values of the threshold angle in these examples (between 20 and 30°) are selected based on observations on the patterns and crack directions from tests performed by Page³⁹ and on the brick pattern of the modeled walls. For walls LOWSTA and HIGSTA the angle of perfect step-wise diagonal cracks would be 46.12°, while for walls TUD-COMP-4 and TUD-COMP-6 it would be 37.6°. The adopted threshold angles ensured that shear behavior would be considered for the angle following from the geometrical brick pattern. Whether the proposed values of the threshold angle are appropriate in the case of bond types other than the stretcher bond considered in the examples herein should be further investigated, because for such bond patterns different angles of the shear cracks may be observed.

5 | CONCLUSIONS

A new plane-stress orthotropic continuum constitutive model for in-plane behavior of masonry structures was developed and presented in this article. The model is based on a total-strain formulation, assuming coaxiality of stresses and strains (rotating crack model). It includes failures in tension, compression, and, indirectly, shear. The postpeak and the unloading/reloading behaviors for tension depend on the principal strain orientation at the onset of cracking. Brittle failure with steep softening is assumed for angles that correspond to in-plane flexural failure, whereas ductile behavior with softening is assumed for angles that correspond to diagonal shear failure. Reduction of the compressive strength due to lateral cracking is adopted, but the increase of the compressive strength due to lateral compression is not accounted for. Additionally, the shear failure is included through a shear-limitation algorithm that limits the stresses based on a Coulomb friction criterion, while maintaining coaxiality between principal stresses and strains and assuming that the confining vertical stress, normal to the bed-joints, remains unchanged. Fifteen input material parameters are required to define the constitutive equations, derived from standard tests performed perpendicularly and in-parallel to the bed joints. In future research, the sensitivity of the model to the number of input parameters will be examined further, and the current plane-stress implementation will be extended to shell elements in order to include out-of-plane failure.

The model was validated against cyclic experimental tests performed on walls with different aspect ratios, boundary conditions and precompression levels. Good agreement was found between the numerical and experimental results, especially in terms of base shear capacity (2%–8%) and sharpness of the crack localization. The model was demonstrated to be able to capture the cyclic hysteretic response in an adequate manner, compared to the performance of fully secant-driven smeared crack or damage based models, or fully elastic unloading/reloading driven plasticity based models, as presented in previous works (e.g., References 18,20,22). The energy dissipation was estimated satisfactorily for walls where a combination of failure modes was observed (flexure and shear cracks, shear and crushing), while the dissipation was underestimated when only pure shear failure was observed, and overestimated when rocking was observed. Results were demonstrated to be sufficiently mesh-insensitive. Only small differences were observed in the prediction of the base shear capacity and crack pattern, while some larger differences occurred in the postpeak regime,

especially between quadratic and linear elements. Nevertheless, there are aspects of the model that still need to be improved, such as the numerical stability, which is heavily influenced by the internal iterative shear loop, as well as the underestimation of the dissipated energy under pure shear. One more aspect that will be investigated further in the future is the limitation of the compressive capacity due to the internal shear loop that might lead to premature crushing.

Overall, the proposed cyclic constitutive model predicts the correct failure mechanism and accurately computes the load-displacement behavior and presenting realistic localized crack patterns for both slender and squat walls. This makes the model an attractive option for the modeling of in-plane unreinforced masonry walls.

ACKNOWLEDGMENTS

This research was funded by Nederlandse Aardolie Maatschappij (NAM) BV under contract number UI46268 “Physical testing and modeling–Masonry structures Groningen”, which is gratefully acknowledged.

ORCID

Marianthi Sousamli  <https://orcid.org/0000-0001-5402-5877>

REFERENCES

- Lagomarsino S, Penna A, Galasco A, Cattari S. TREMURI program: an equivalent frame model for the nonlinear seismic analysis of masonry buildings. *Eng Struct*. 2013;56:1787-1799.
- Siano R, Sepe V, Camata G, Spacone E, Roca P, Pelà L. Analysis of the performance in the linear field of equivalent-frame models for regular and irregular masonry walls. *Eng Struct*. 2017;145:190-210.
- Bracchi S, Graziotti F, Messali F, Penna A. Seismic assessment of Dutch URM buildings according to Npr9998:2018 code with an equivalent-frame approach. International Centre for Numerical Methods in Engineering, CIMNE; 2021.
- Cundall PA, Hart RD. Numerical modelling of discontinua. *Eng Comput*. 1992;9:101-113.
- Lemos JV. Discrete element modeling of masonry structures. *Int J Arch Heritage*. 2007;1:190-213.
- Malomo D, Pinho R, Penna A. Using the applied element method for modelling calcium silicate brick masonry subjected to in-plane cyclic loading. *Earthq Eng Struct Dyn*. 2018;47:1610-1630.
- Malomo D, DeJong MJ, Penna A. Distinct element modelling of the in-plane cyclic response of URM walls subjected to shear-compression. *Earthq Eng Struct Dyn*. 2019;48:1322-1344.
- Hrvoje S, Nikolina Ž, Željana N. A combined finite-discrete element analysis of dry stone masonry structures. *Eng Struct*. 2013;52:89-100.
- Paola Costanza M, Evan CB, Giovanni G. Finite/discrete element modelling of reversed cyclic tests on unreinforced masonry structures. *Eng Struct*. 2017;138:159-169.
- Malomo D, DeJong MJ. A macro-distinct element model (M-DEM) for simulating the in-plane cyclic behavior of URM structures. *Eng Struct*. 2021;227:111428.
- Minga E, Macorini L, Izzuddin BA. A 3D mesoscale damage-plasticity approach for masonry structures under cyclic loading. *Meccanica*. 2018;53:1591-1611.
- Alfano G, Sacco E. Combining interface damage and friction in a cohesive-zone model. *Int J Numer Methods Eng*. 2006;68:542-582.
- Lotfi HR, Shing PB. Interface model applied to fracture of masonry structures. *J Struct Eng*. 1994;120:63-80.
- D’Altri AM, de Miranda S, Castellazzi G, Sarhosis V. A 3D detailed micro-model for the in-plane and out-of-plane numerical analysis of masonry panels. *Comput Struct*. 2018;206:18-30.
- Bertolesi E, Milani G, Lourenço PB. Implementation and validation of a total displacement non-linear homogenization approach for in-plane loaded masonry. *Comput Struct*. 2016;176:13-33.
- Calderini C, Lagomarsino S. Continuum model for in-plane anisotropic inelastic behavior of masonry. *J Struct Eng-Asce*. 2008;134:209-220.
- Zucchini A, Lourenço PB. A micro-mechanical homogenisation model for masonry: application to shear walls. *Int J Solids Struct*. 2009;46:871-886.
- Schreppers GMA, Garofano A, Messali F, Rots JG. *DIANA Validation Report for Masonry Modelling*. DIANA FEA BV & TU Delft; 2016.
- Lotfi H, Shing P. An appraisal of smeared crack models for masonry shear wall analysis. *Comput Struct*. 1991;41:413-425.
- Berto L, Saetta A, Scotta R, Vitaliani R. An orthotropic damage model for masonry structures. *Int J Numer Methods Eng*. 2002;55:127-157.
- Pelà L, Cervera M, Oller S, Chiumenti M. A localized mapped damage model for orthotropic materials. *Eng Fract Mech*. 2014;124:196-216.
- Gambarotta L, Lagomarsino S. Damage models for the seismic response of brick masonry shear walls. Part II: the continuum model and its applications. *Earthq Eng Struct Dyn*. 1997;26:441-462.
- Saloustros S, Pelà L, Cervera M, Roca P. An enhanced finite element macro-model for the realistic simulation of localized cracks in masonry structures: a large-scale application. *Int J Arch Heritage*. 2018;12:432-447.
- Lourenço PB, de Borst R, Rots JG. A plane stress softening plasticity model for orthotropic materials. *Int J Numer Methods Eng*. 1997;40:4033-4057.

25. Papa E, Nappi A. Numerical modelling of masonry: a material model accounting for damage effects and plastic strains. *App Math Model.* 1997;21:319-335.
26. Lee J, Fenves GL. Plastic-damage model for cyclic loading of concrete structures. *J Eng Mech.* 1998;124:892-900.
27. Lubliner J, Oliver J, Oller S, Oñate E. A plastic-damage model for concrete. *Int J Solids Struct.* 1989;25:299-326.
28. Oliveira DV, Lourenço PB. Implementation and validation of a constitutive model for the cyclic behaviour of interface elements. *Comput Struct.* 2004;82:1451-1461.
29. Feenstra PH, Rots JG, Arnesen A, Teigen JG, Hoiseth KV. A 3D constitutive model for concrete based on a co-rotational concept. Proceedings of the Euro-C Conference Computational Modelling of Concrete Structures; 1998; Balkema.
30. Jirásek M, Zimmermann T. Analysis of rotating crack model. *J Eng Mech.* 1998;124:842-851.
31. Jafari S, Rots JG, Esposito R, Messali F. Characterizing the material properties of Dutch unreinforced masonry. *Proc Eng.* 2017;193:250-257.
32. Naraine K, Sinha S. Behavior of brick masonry under cyclic compressive loading. *J Struct Eng-Asce.* 1989;115:1432-1445.
33. Page A. An experimental investigation of the biaxial strength of brick masonry. *Proceedings of the Sixth International Brick Masonry Conference (Rome).* 1982:3-15.
34. Atkinson RH, Amadei BP, Saeb S, Sture S. Response of masonry bed joints in direct shear. *J Struct Eng-Asce.* 1989;115:2276-2296.
35. Van der Pluijm R. Non-linear behaviour of masonry under tension. *Heron-English Edition.* 1997;42:25-54.
36. (NEN) KNNI NPR 9998:2020 en. Assessment of structural safety of buildings in case of erection, reconstruction and disapproval induced earthquakes - Basis of Design, Actions and Resistances; 2021.
37. van der Pluijm R. *Out-of-Plane Bending of Masonry: Behaviour and Strength.* Doctor of Philosophy. Eindhoven: Technische Universiteit Eindhoven; 1999.
38. CEN. Eurocode 6: design of masonry structures—part 1–1: general rules for reinforced and unreinforced masonry structures. Standardisation ECF, editor. EN 1996-1-1; 2005; Brussels, Belgium.
39. Page AW. The biaxial compressive strength of brick masonry. *Proc Inst Civil Eng.* 1981;71:893-906.
40. Dhanasekar M, Page A, Kleeman P. The failure of brick masonry under biaxial stresses. *Proc Inst Civil Eng.* 1985;79:295-313.
41. Messali F, Esposito R, Ravenshorst G, Rots J. Experimental investigation of the in-plane cyclic behaviour of calcium silicate brick masonry walls. *Bull Earthq Eng.* 2020;18:1-32.
42. Bažant ZKP, Oh BH. Crack band theory for fracture of concrete. *Matériaux et Construct.* 1983;16:155-177.
43. Govindjee S, Kay GJ, Simo JC. Anisotropic modelling and numerical simulation of brittle damage in concrete. *Int J Numer Methods Eng.* 1995;38:3611-3633.
44. Oliver J. A consistent characteristic length for smeared cracking models. *Int J Numer Methods Eng.* 1989;28:461-474.
45. Rots JG, Nauta P, Kuster GMA, Blaauwendraad J. Smeared crack approach and fracture localization in concrete. *Heron.* 1985;30(1):1985.
46. Hoshikuma J, Kawashima KMA, Nagaya K, Taylor AWMA. Stress-strain model for confined reinforced concrete in bridge piers. *J Struct Eng.* 1997;123(5):624-633.
47. Facconi L, Minelli F, Vecchio FJ. Predicting uniaxial cyclic compressive behavior of brick masonry: new analytical model. *J Struct Eng.* 2018;144:04017213.
48. Ispir M, Ilki A. Behavior of historical unreinforced brick masonry walls under monotonic and cyclic compression. *Arab J Sci Eng.* 2013;38:1993-2007.
49. Naraine K, Sinha S. Cyclic behavior of brick masonry under biaxial compression. *J Struct Eng.* 1991;117:1336-1355.
50. Thamboo J, Bandara J, Perera S, Navaratnam S, Poologanathan K, Corradi M. Experimental and analytical study of masonry subjected to uniaxial cyclic compression. *Materials.* 2020;13:4505.
51. Oliveira DV, Lourenço PB, Roca P. Cyclic behaviour of stone and brick masonry under uniaxial compressive loading. *Mater Struct.* 2006;39:247-257.
52. Segura J, Pelà L, Roca P. Monotonic and cyclic testing of clay brick and lime mortar masonry in compression. *Construct Build Mater.* 2018;193:453-466.
53. Lee S-J, Eom T-S, Yu E. Investigation of diagonal strut actions in masonry-infilled reinforced concrete frames. *Int J Concr Struct Mater.* 2021;15:1-14.
54. Vecchio FJ, Collins MP. Compression response of cracked reinforced-concrete. *J Struct Eng-Asce.* 1993;119:3590-3610.
55. Rahman A, Ueda T. Experimental investigation and numerical modeling of peak shear stress of brick masonry mortar joint under compression. *J Mater Civil Eng.* 2014;26:04014061.
56. Lourenço PB, Rots JG. Understanding the behaviour of shear walls: a numerical approach. Proceedings of the 10 th International Brick/Block Masonry Conference; 1994; Calgary.
57. van Zijl GPAG. Modeling masonry shear-compression: role of dilatancy highlighted. *J Eng Mech.* 2004;130:1289-1296.
58. Rots JG. *Computational Modeling of Concrete Fracture.* Delft University of Technology; 1988.
59. Anthoine A, Magonette G, Magenes G. Shear-compression testing and analysis of brick masonry walls. In: Duma G, ed. *Proceedings of the 10th European Conference on Earthquake Engineering.* IEEE; 1994:1657-1662.
60. Magenes G, Calvi GM. In-plane seismic response of brick masonry walls. *Earthq Eng Struct Dyn.* 1997;26:1091-1112.
61. Binda L, Tiraboschi C, Mirabella Roberti G, Baronio G, Cardani G. Measuring masonry material properties: detailed results from an extensive experimental research, Part I: tests on masonry components. *Rep.* 1996;5.

62. Magenes G, Calvi GM. Cyclic behaviour of brick masonry walls. Proceedings of the 10th World Conference on Earthquake Engineering; 1992:3517-3522; Madrid.
63. Lourenço PB. Computations on historic masonry structures. *Progr Struct Eng Mater*. 2002;4:301-319.
64. Jirásek M, Bauer M. Numerical aspects of the crack band approach. *Comput Struct*. 2012;110-111:60-78.

How to cite this article: Sousamli M, Messali F, Rots JG. A total-strain based orthotropic continuum model for the cyclic nonlinear behavior of unreinforced brick masonry structures. *Int J Numer Methods Eng*. 2022;1-28. doi: 10.1002/nme.6917